Dynamic stall of a pitching airfoil under reverse flow conditions

Xu, G.; Sciacchitano, A.; Simao Ferreira, Carlos; Yu, W.

DOI
10.1063/5.0294915

Publication date
2025

Document Version
Final published version

Published in
Physics of Fluids

Citation (APA)
Xu, G., Sciacchitano, A., Simao Ferreira, C., & Yu, W. (2025). Dynamic stall of a pitching airfoil under reverse flow conditions. *Physics of Fluids*, *37*(11), Article 117139. https://doi.org/10.1063/5.0294915

Physics of Fluids

RESEARCH ARTICLE | NOVEMBER 26 2025

Dynamic stall of a pitching airfoil under reverse flow conditions

Guanqun Xu (徐冠群) ; Andrea Sciacchitano ; Carlos Ferreira ; Wei Yu (余畏)

Physics of Fluids 37, 117139 (2025)
https://doi.org/10.1063/5.0294915

AIP Publishing

Physics of Fluids ARTICLE pubs.aip.org/aip/pof

Dynamic stall of a pitching airfoil under reverse flow conditions

Cite as: Phys. Fluids **37**, 117139 (2025); doi: 10.1063/5.0294915
Submitted: 6 August 2025 · Accepted: 30 October 2025 ·
Published Online: 26 November 2025

Guanqun Xu (徐冠群),[a] Andrea Sciacchitano, Carlos Ferreira, and Wei Yu (余畏)

AFFILIATIONS

Faculty of Aerospace Engineering, Delft University of Technology, Delft, South Holland, the Netherlands

[a]Author to whom correspondence should be addressed: G.Xu-1@tudelft.nl

ABSTRACT

This study experimentally investigates the dynamic stall of a pitching NACA 643418 airfoil under reverse flow conditions, whereby the geometric trailing edge is located upstream of the geometric leading edge. The investigation focuses on the correlation between surface pressure, aerodynamic forces, and the evolution of the dynamic stall vortex (DSV) and the aerodynamic trailing edge vortex (TEV). A range of mean angles of attack from 5° to 25°, pitching amplitudes from 5° to 15°, and reduced frequencies between 0.05 and 0.21 were tested on an airfoil using a combination of particle image velocimetry (PIV) and surface pressure measurements. The results reveal a distinct dynamic stall mechanism in reverse flow conditions: multiple flow separations occur during both the upstroke and downstroke periods, yet the DSV maintains partial attachment. While the outer layer of the DSV sheds into the flow, its inner core remains anchored and is subsequently reinforced by shear layer feeding. This sustained vorticity injection leads to periodic DSV re-growth, which manifests in the force hysteresis loop as multiple distinct peak regions. In addition, it is also found that the largest difference between conventional and reverse flow dynamic stall lies in the initial stage of the DSV development. For reverse flow dynamic stall cases, the initial flow separation near the leading edge causes a gradual decrease in the pressure coefficient. However, for conventional dynamic stall cases, the laminar separation bubbles that occur before the DSV cause the maximum suction on the airfoil surface. Furthermore, by comparing the dominant modes from Proper Orthogonal Decomposition (POD) analysis, it is found that the type of flow regime depends mainly on the mean angle of attack within the tested range of pitching amplitudes and frequencies. In particular, the dominant vortex determines the flow dynamics. At low mean angles of 5° and 10°, the most energetic flow features are associated with DSV dynamics. At a mean angle of 15°, both DSV and TEV dynamics contribute. At higher mean angles of 20° and 25°, the flow is dominated more by TEV dynamics. Despite these mean-angle-dependent variations in modal dominance, all dominant POD modes share a consistent physical interpretation where they capture the growth or decay of DSV and TEV structures.

I. INTRODUCTION

Dynamic stall appears in a wide range of aerodynamic applications such as helicopters, rapidly maneuvering aircraft, wind turbines, and insect wings.[1] It occurs when a lifting surface undergoes rapid changes in the angle of attack, leading to unsteady flow separation, vortex formation, and shedding. These processes significantly impact aerodynamic performance, often resulting in large unsteady loads, vibrations, fatigue, and potential structural damage. Understanding dynamic stall is, therefore, essential for optimizing the design and operation of aerodynamic systems, particularly under unsteady conditions.

Highly influential pioneering work from the 1970s to the 1990s provides not only a wide range of experimental studies on the forces and vortex dynamics during dynamic stall (see McCroskey and Fisher,[2] Carr,[1] McCroskey,[3] and Mcalister *et al.*[4]) but also widely used numerical models for dynamic stall (see Leishman and Beddoes,[5] Truong,[6] and Tran and Petot[7]). In recent years, research on dynamic stall has continued to advance, with a strong focus on conventional flow conditions. Akbari and Price[8] applied a vortex method to simulate a pitching NACA 0012 airfoil under dynamic stall conditions, where the effects of pitching parameters of reduced frequency, mean angle of attack, location of pitch axis, and Reynolds numbers were investigated. Mulleners and Raffel[9] conducted an experimental investigation of a pitching airfoil with dynamic stall, employing various numerical methods to identify coherent flow structures. Their work classified dynamic stall into distinct stages based on the life cycle of dynamic stall vortices, providing significant insights into vortex development. Building on this, Mulleners and Raffel[10] further explored the vortex dynamics and flow mechanisms during dynamic stall, identifying primary and secondary instabilities. Similarly, Gupta and Ansell[11] experimentally studied the unsteady flow physics of a dynamic pitching airfoil, with a particular focus on the airfoil boundary layer, leading-edge laminar separation bubble, and dynamic stall vortex. Kiefer *et al.*[12] expanded on these findings by conducting experimental measurements on a ramp-type pitching airfoil, revealing universal pressure patterns independent of parameter variations of mean angle, ramp angle amplitude, Reynolds number, and reduced frequency. Their study also emphasized the impact of Reynolds number and reduced frequency on dynamic stall behavior, demonstrating that the angle of attack during pitching relative to the static stall angle, which depends on Reynolds number, plays a key role in the temporal progression of the stall process. Additionally, they found that once a critical reduced frequency is reached, both the load magnitude and the vortex evolution become independent of further increases in the reduced frequency. Collectively, these works provide a detailed picture of vortex formation, force variation, and parameter sensitivity in conventional forward-flow dynamic stall.

In contrast, dynamic stall under reverse flow conditions, where the geometric trailing edge faces the incoming flow, remains far less understood. Meanwhile, reverse flow dynamic stall has been documented in helicopter applications.[13,14] For wind turbines, this phenomenon is critical during parked conditions or during installation, as omnidirectional wind exposure can trigger vortex-induced vibrations (VIV) and significantly accelerate fatigue damage. However, the fundamental flow mechanisms governing reverse flow dynamic stall remain unsolved, leaving a critical gap in our ability to address these operational challenges.

One of the most defining features of dynamic stall, whether under conventional or reverse flow conditions, is the development of the dynamic stall vortex (DSV). The DSV typically forms near the aerodynamic leading edge, grows in size as it convects downstream, and eventually detaches from the airfoil surface, causing significant variations in aerodynamic forces and moments. In conventional cases, this process is well-documented and characterized by strong hysteresis effects in lift, drag, and pitching moment. Guillaud *et al.*[15] numerically investigated a pitching airfoil under forward flow conditions and observed that as the reduced frequency[16] (defined as $2\pi f * (c/2)/U_\infty$, where f is the pitching frequency in Hz, c is the chord length of the airfoil, and U_∞ is the incoming wind speed) increases, the leading-edge vortex (LEV) exhibits a shorter life span, although its formation and shedding occur over a larger range of angles of attack. This behavior results in a more abrupt force drop at higher reduced frequencies. Wei *et al.*[17] studied a conventional dynamic stall setup, where the near-wall development characteristics and near-wall evolution velocity are studied in detail. From their pressure measurement, it is found that two LEVs are formed at different locations on the airfoil surface, which then develop together into a DSV. Khalifa *et al.*[18] numerically studied the dynamic stall on a pitching NACA 0012 airfoil, where the interaction between multiple LEVs and turbulent separated vortices is captured. By contrast, for reverse flow dynamic stall, much less is known. Lind and Jones[19] observed the formation of two DSVs in a single cycle, with fewer vortices at higher reduced frequency, attributing the secondary force peak to weaker vortex shedding. Yet, without detailed flow-field validation, such interpretations remain tentative. Thus, while DSV dynamics in conventional stall are now well established, their manifestation in reverse flow conditions is still an open question, which directly motivates the present study.

Motivated by these gaps, the present study investigates experimentally the dynamic stall phenomenon under reverse flow conditions. The main goal is to study the vortex dynamics, surface pressure distribution, force variation, and the dominant flow feature during reverse-flow dynamic stall. The analysis is based on both the surface static pressure measurements and the particle image velocimetry (PIV) flow field measurements. The structure of the paper is as follows: in Sec. II, the experimental design and setup are introduced, followed by wind tunnel data correction methods used in the study. Then, in Sec. III, the pressure measurement results and PIV flow fields are compared and analyzed for the tested dynamic stall cases. Afterward, the most energetic flow structures in the different pitching conditions are investigated by means of Proper Orthogonal Decomposition (POD) analysis. Finally, the main conclusions of this work are reported in Sec. IV.

II. METHODOLOGY

A. Definitions and nomenclature in reverse flow dynamic stall conditions

To analyze reverse-flow dynamic stall systematically and to better compare with conventional dynamic stall cases, it is essential to define the key parameters and conventions for an airfoil under reverse flow conditions.

First of all, the angle of attack during a reverse flow dynamic stall α is defined as $\alpha = 180° - \alpha'$, where α' is the nominal angle of attack in degrees defined in many fundamental books, such as those by Anderson.[20] In this paper, each case is labeled as $\overline{\alpha}a_1\Delta a_2 k a_3$ (or $\overline{\alpha'}a_1\Delta a_2 k a_3$ for conventional dynamic stall cases), where $\overline{\alpha}$ (or $\overline{\alpha'}$) is the mean angle of attack during pitching, Δ is a shorter symbol for the pitching amplitude ($\Delta\alpha$), and k is the reduced frequency. k is defined as $2\pi f * (c/2)/U_\infty$,[16] where f is the pitching frequency in Hz, c is the chord length of the airfoil in meters, and U_∞ is the incoming wind speed in meters per second. Finally, a_1, a_2, and a_3 indicate the specific numerical values of $\overline{\alpha}$ (in °), $\Delta\alpha$ (in °), and k separately.

Figure 1 shows the schematic plot of the airfoil orientation at case $\overline{\alpha}10\Delta10k0.1$ compared to a reference orientation where $\alpha' = 0°$. The pitching airfoil reaches the minimum angle of $\alpha_{min} = 0°$ and the maximum angle of $\alpha_{max} = 20°$. The cross in the figure represents the location of the physical pitching axis, which is at $x_c/c = 0.4012$. x_c denotes the chordwise coordinate along the airfoil, where $x_c/c = 0$ is the geometric leading edge. The wind comes from the left. Under this

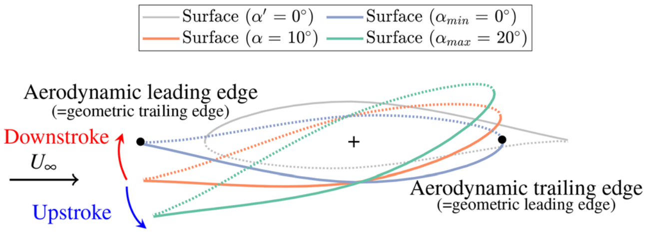

FIG. 1. Schematic plot of airfoil orientation at case $\overline{\alpha}10\Delta10k0.1$. Solid lines represent the suction side of the airfoil surface, while the dotted lines represent the pressure side. Arrows indicate pitching motion directions. The aerodynamic leading and trailing edges are indicated with black dots.

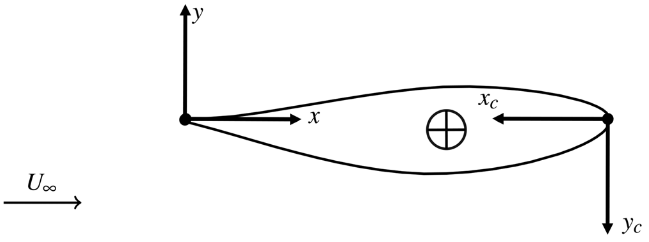

FIG. 2. Illustration of the two coordinate systems used in the study.

reverse flow condition, the geometric trailing edge becomes the aerodynamic leading edge. For clarification, if not specified, the leading edge and trailing edge mentioned in the rest of the paper are referred to as the aerodynamic leading edge and aerodynamic trailing edge, respectively. In addition, in order to make a fair comparison with conventional dynamic stall cases, in the reverse flow dynamic stall condition, the upstroke motion is defined as when α increases (aerodynamic leading edge moving down), and the downstroke motion is defined as when α decreases (aerodynamic leading edge moving up).

During the pitching motion of the airfoil, two coordinate systems are defined as shown in Fig. 2, where x and y are the global coordinate system with x aligning with the free-stream direction, and x_c and y_c follow the airfoil coordinate system, where x_c aligns with the chordline of the airfoil. The origin in the airfoil coordinate system is located at the geometric leading edge, which aligns with the conventional airfoil convention. Instead, the origin of the global coordinate system is positioned at the location of the geometric trailing edge when $\alpha = 0°$ ($\alpha' = 180°$).

The aerodynamic lift coefficient C_l and the aerodynamic moment coefficient C_m are analyzed in this study. These results are obtained from the integration of the measured pressure using equations reported in chapter 1 of Anderson's book.[20]

B. Experimental design and setup

1. Wind tunnel and model

The experiments were conducted in the low-speed low turbulence tunnel (LTT) at the Delft University of Technology in the Netherlands. The LTT is a closed-test section, closed-circuit wind tunnel with a nominal turbulence intensity varying from 0.015% at 20 m/s to 0.07% at 75 m/s and an octagonal test section 1.80 m wide, 1.25 m high, and 2.60 m long. A wing with a NACA 643418 profile was used in the experiments. The wing spans the entire vertical dimension of the test section (1.25 m) and has a chord length of 250 mm, leading to an aspect ratio of 5. A total of 49 pressure sensors were used to measure the static pressure over the airfoil surface. The airfoil geometry and pressure tap locations are shown in Fig. 3.

2. Pressure measurement

The surface pressure was measured using the Digital Temperature Compensation (DTC) Initium electronic pressure scanning system, which supports up to eight DTC scanners to facilitate as many as 512 channels of pressure measurements. The accuracy is ±0.05% for a full-scale range (>5 psid) measurement. The system can measure at a maximum frequency of 1200 Hz when scanning 16 channels per scanner. In this campaign, the acquisition frequency was set to 300 Hz.

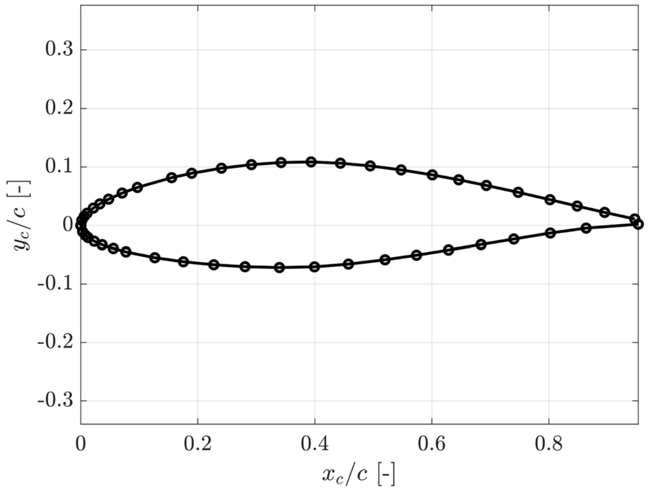

FIG. 3. Shape of the NACA643418 airfoil, together with the location of the pressure taps.

The test matrix for reverse flow dynamic stall conditions is shown in Table I, where the chord-based Reynolds number Re was set at 2.5×10^5 and the free stream velocity (U_∞) is approximately 14.9 m/s. The design of the test matrix is explained in the appendix. Additionally, a few conventional cases are also tested, with the test matrix shown in Table II. The number of cycles required for each test case was determined through a convergence study. One pitching case was measured over a duration of 299 cycles, with each cycle consisting of one upstroke and one downstroke. The standard deviation was evaluated for comparisons between 50 and 298 cycles. Note that the first cycle was excluded from the standard deviation calculation to avoid transient effects in the measurement. Further details can be found in Appendix A. Based on the study, 150 cycles were selected for each test case to ensure high accuracy while minimizing test duration. The results presented in this study are based on the 149 cycles following the excluded first cycle.

TABLE I. Test matrix of the experimental campaign for reverse flow conditions.

$\overline{\alpha}$ (°)	$\Delta\alpha$ (°)	f (Hz)	k (–)
5, 10, 15, 20, 25	5	1, 2, 3, 4	0.05, 0.1, 0.16, 0.21
	10	1, 1.5, 2, 2.5, 3, 3.5	0.05, 0.08, 0.1, 0.13, 0.16, 0.18
	15	1, 2, 3	0.05, 0.1, 0.16[a]

[a] The case with $k = 0.16$ at $\Delta\alpha = 15°$ was only tested at $\overline{\alpha} = 20°$ and 25° due to experimental constraints.

TABLE II. Test matrix of the experimental campaign for conventional cases.

$\overline{\alpha'}$ (°)	$\Delta\alpha$ (°)	f (Hz)	k (–)
5, 10, 15	5	1, 2, 3, 4	0.05, 0.1, 0.16, 0.21
	10,15[a]	1, 2, 3	0.05, 0.1, 0.16

[a] Instead of $\Delta\alpha = 15°$, the case with $\overline{\alpha'} = 15°$ was tested with $\Delta\alpha = 14°$ due to experimental constraints.

To represent the uncertainty of the pressure measurement, we calculate the 95% confidence interval for the mean value of lift coefficient C_l and moment coefficient C_m over 149 cycles. The following procedure shows an example of uncertainty calculation for C_l.

First of all, the standard deviation of C_l (σ_{C_l}) is calculated as

$$\sigma_{C_l} = \sqrt{\frac{1}{n-1}\sum_{i=1}^{n}\left(C_{l,i} - \overline{C_l}\right)^2},$$

where n is the number of cycles, $C_{l,i}$ is the C_l time series at the i's cycle, and $\overline{C_l}$ is the cycle-averaged C_l.

Then the standard error (SE) of the mean value is calculated as

$$\mathrm{SE} = \frac{\sigma_{C_l}}{\sqrt{n}}.$$

Assuming the data are approximately normally distributed, the 95% confidence interval for the mean $\overline{C_l}$ is given by

$$C_{l_{95\%}} = \overline{C_l} \pm t_{0.975,df} \cdot \mathrm{SE},$$

where $t_{0.975,df}$ is the critical value from the Student's t-distribution,[21] with $df = n - 1$ degrees of freedom (reflecting the number of independent observations used to estimate the variance), corresponding to the two-sided 95% confidence interval. For $n = 149$, this value is $t_{0.975,df} = 1.976$.

3. Particle image velocimetry (PIV)

PIV measurements were conducted using the apparatus shown schematically in Fig. 4. The flow inside the tunnel was seeded with water–glycol droplets of 1 μm median diameter produced by a SAFEX smoke generator. The flow was illuminated by two Quantel Evergreen Nd:YAG lasers (200 mJ pulse energy, maximum 15 Hz repetition rate, 532 nm wavelength), shooting from the two sides of the test section to illuminate both pressure and suction sides of the airfoil. Flow field imaging was conducted using two LaVision Imager sCMOS cameras (2560×2160 pixel, 16 bit, $6.5 \times 6.5\,\mu\mathrm{m}^2$ pixel size) equipped with 50-mm Nikon lenses; the lens numerical aperture was set to $f = 8$. The optical magnification was $M = 0.03$, yielding a digital image resolution of 4.94 pixels/mm. The cameras were controlled by a LaVision programmable timing unit PTU X, where precise pulses are triggered and synchronized for cameras and lasers.

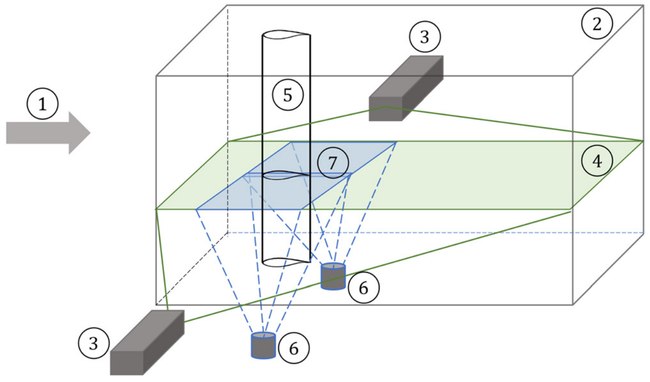

FIG. 4. Schematic plot of the PIV setup with reference directions. The components of the measurement are ① incoming wind, ② test section, ③ lasers, ④ illumination plane, ⑤ airfoil model, ⑥ cameras, and ⑦ field of view.

Based on the convergence analysis shown in Appendix A in Fig. 26, 50 cycles yield a low standard deviation of less than 2.5%. Therefore, in order to maintain a high efficiency while measuring, for PIV measurements, 50 pairs of images were taken for each phase. The field of view (FoV) has a size of approximately 430×363 mm^2. The images were first filtered with a Butterworth high-pass filter[22] with a filter length of seven images. Then the vector calculation is performed with two rounds of passes: the initial pass has an interrogation window size of 128×128 pixel, with an overlap ratio of 50%; the second pass has an interrogation window size of 32×32 pixel, with an overlap ratio of 75%. The last pass gives the vector pitch of 1.343 mm.

The uncertainty in the PIV measurements is determined based on the ensemble data size and the flow velocity fluctuations, as outlined by Ye *et al.*[23] For each measured phase, 50 uncorrelated snapshots were collected, resulting in the standard uncertainty of the phase-averaged flow velocity being given by

$$\varepsilon_{\overline{u}} = \frac{\sigma_u}{U_\infty \sqrt{N}}. \qquad (1)$$

σ_u is the representative standard deviation value of the streamwise velocity component (σ_u / U_∞ is approximately 0.1 in the airfoil's wake), and N represents the number of uncorrelated samples. This equation yields $\varepsilon_{\overline{u}} \approx 1.4\%$ for the present experiment.

The uncertainty of the root mean square of the velocity fluctuations is estimated as (Sciacchitano and Wieneke[24])

$$\varepsilon_{u'} = \frac{\sigma_u}{U_\infty \sqrt{2(N-1)}}. \qquad (2)$$

The expression yields $\varepsilon_{u'} \approx 0.1\%$.

C. Data processing

1. Unsteady pressure measurement correction

When measuring unsteady pressure, delays and damping effects are often observed due to the geometric characteristics of the pressure tubes and sensors. To address this, one approach is to apply a transfer function to correct the data in the frequency domain based on the theoretical framework developed by Bergh and Tijdeman.[25] The theory assumes that (1) the sinusoidal disturbances are very small, (2) the internal radius of the tube is small compared to its length, and (3) the flow is laminar throughout the system.

For N connected tubes with N volumes as shown in Fig. 5, a recursive formula for the pressure P in volume j can be derived as

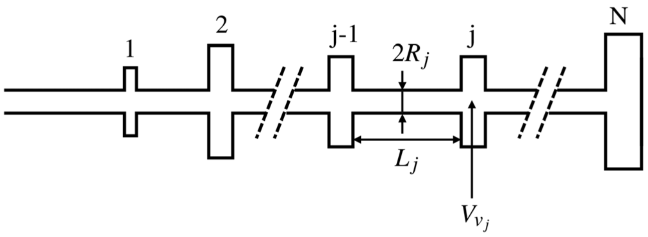

FIG. 5. A series of N connected tubes with N different volumes at the end of each tube. R_j represents the tube radius.

$$\frac{P_j}{P_{j-1}} = \begin{cases} \Bigg[\cosh(\phi_j L_j) + \dfrac{V_{v_j}}{V_{t_j}}\left(\sigma_j + \dfrac{1}{k_{0,j}}\right) n_j \phi_j L_j \sinh(\phi_j L_j) \\ \quad + \dfrac{V_{t_{j+1}}\phi_{j+1} L_j J_0(\alpha_j) J_2(\alpha_{j+1})}{V_{t_j}\phi_j L_{j+1} J_0(\alpha_{j+1}) J_2(\alpha_j)} \cdot \dfrac{\sinh(\phi_j L_j)}{\sinh(\phi_{j+1} L_{j+1})} \\ \quad \cdot \left(\cosh(\phi_{j+1} L_{j+1}) - \dfrac{P_{j+1}}{P_j}\right)\Bigg]^{-1} & \text{if } j < N, \\ \cosh(\phi_j L_j) + \dfrac{V_{v_j}}{V_{t_j}}\left(\sigma_j + \dfrac{1}{k_{0,j}}\right) n_j \phi_j L_j \sinh(\phi_j L_j) & \text{if } j = N, \end{cases} \tag{3}$$

where L is the tube length, V_v is the pressure transducer volume, V_t is the tube volume, σ is the dimensionless increase in transducer volume due to diaphragm deflection, k_0 is the polytropic constant for the pressure expansion in the transducer volume, equaling to 1.4 for isentropic pressure expansion, and J_0 and J_2 are Bessel functions of first kind of orders 0 and 2.

In addition, ϕ_j, α_j (shear wave number), n_j (kind of polytropic constant) are calculated as

$$\phi_j = \frac{\omega}{a_0}\sqrt{\frac{J_0(\alpha_j)\,\gamma}{J_2(\alpha_j)\,n_j}}, \tag{4}$$

$$\alpha_j = i\sqrt{i}\sqrt{\frac{\omega\,\mathrm{P}_m}{R_0\,T\,\mu}}R_j, \tag{5}$$

$$n_j = \left[1 + \frac{\gamma - 1}{\gamma}\cdot\frac{J_2\left(\alpha_j\sqrt{\mathrm{Pr}}\right)}{J_0\left(\alpha_j\sqrt{\mathrm{Pr}}\right)}\right]^{-1}, \tag{6}$$

where ω is the angular frequency, P_m is the atmospheric pressure, R is the tube radius, R_0 is the specific air constant, which is 287 J/kg K, T is the ambient air temperature, μ is the dynamic viscosity of air, γ is the specific heat ratio, which is equal to the ratio between the specific heat at constant pressure and the specific heat at constant volume, and Pr is the Prandtl number.

After Eq. (3) is obtained, the phase delay and the amplitude ratio between the corrected and uncorrected pressure can be calculated by taking the absolute value and the angle value of the response.

2. Wind tunnel wall correction

Due to the presence of wind tunnel walls in a closed test section, the flow conditions are different compared to free-air conditions. Therefore, corrections should be applied to the raw pressure data, accounting for the lift interference, blockage, and wake buoyancy. Similarly to Xu *et al.*,[26] two correction methods were applied depending on the angle of attack: the method from Timmer[27] for instantaneous angles of attack not exceeding 20° (mainly for the static measurement as shown in Fig. 27 in Appendix A); the method from Maskell[28] for higher angles of attack.

3. Proper Orthogonal Decomposition (POD)

The Proper Orthogonal Decomposition (POD) is a well-established mathematical method aimed at obtaining low-dimensional approximate descriptions of high-dimensional processes.[29] In flow dynamics, POD is extremely helpful because it extracts the most energetic coherent structures from complex, high-dimensional flow fields. In this study, POD analysis is performed on the airfoil suction side surface pressure. In POD, the original pressure coefficient field $C_p(x_c/c, t)$ is decomposed into a linear combination of spatial modes $[\phi_k(x_c/c)]$ and time coefficients $(a_k(t))$:

$$C_p(x_c/c, t) \cong \sum_{k=1}^{M} a_k(t)\phi_k(x_c/c), \tag{7}$$

where the approximation becomes the exact limit as M (the number of retained POD modes) reaches infinity. The decomposition is derived from solving the eigenvalue problem of the spatial correlation matrix, ensuring that the modes optimally capture the pressure fluctuations.

III. RESULTS AND DISCUSSION

A. Pressure, force, and vortex dynamics during dynamic stall under reverse flow conditions

The analysis begins with a comprehensive examination of pressure fields, integrated aerodynamic forces, and flow structures across all test cases. A detailed discussion is presented of two representative cases: $\overline{\alpha}10\Delta10k0.1$ and $\overline{\alpha}20\Delta10k0.1$, characterized by a different number of suction regions on the airfoil surface.

1. Localized suction region case: $\overline{\alpha}10\Delta10k0.1$

This section discusses the case $\overline{\alpha}10\Delta10k0.1$, where the airfoil is operated at $\overline{\alpha} = 10°$, $\Delta\alpha = 10°$, and $k = 0.1$.

Figure 6(a) presents the cycle-averaged pressure coefficient C_p on the suction side of the airfoil. From the left to right of the plot, the colormap indicates the value of C_p during the upstroke period from $\alpha = 0°$ to $20°$ and then downstroke to $\alpha = 0°$. A schematic airfoil is plotted on the left of the figure with the leading edge $(x_c/c = 1)$ and trailing edge $(x_c/c = 0)$ aligned with the y-axis. This airfoil is oriented at $\alpha = 0°$, and the suction side is marked by the solid line. In the colormap, gray isolines indicate the C_p-levels in increments of $\Delta C_p = 0.25$. Meanwhile, the measured PIV phases are marked with vertical dashed lines, where the vorticity fields are shown in Fig. 7. During the initial upstroke motion from phase *a* (0°) until approximately phase *c* (4.0°), the flow remains attached to the airfoil surface, with the lowest C_p near the highest thickness region $(x_c/c \approx 0.4)$. The vorticity fields from the PIV measurement during these phases are shown in Figs. 7(a)–7(d). Likewise, no major flow event happens, and the flow remains fully attached. The high vorticity in proximity to the airfoil surface is representative of the boundary layers forming on both the pressure and suction sides. Starting approximately at phase *d* and starting from the leading edge, C_p decreases to below zero. This is ascribed to the initiation of the DSV, which grows from the leading edge, where the flow separation (FS) can be seen from the suction side near the leading edge (from phases *d* to *f*). As the suction region grows larger, the DSV is formed as shown at phase *g* [$\alpha = 18.1°$, Fig. 7(g)]. At this phase, the DSV core [$x_c/c = 0.28$, marked by the blue curve in Fig. 6(a)] is visible, which is close to the maximum thickness region of the airfoil. The vortex core location is evaluated using the Γ_1 method.[30,31] The circulation of the DSV is shown in Fig. 6(b), which is obtained by integrating the positive vorticity in the wake of the airfoil region, thus excluding the negative vorticity, which is associated with the TEV. The result

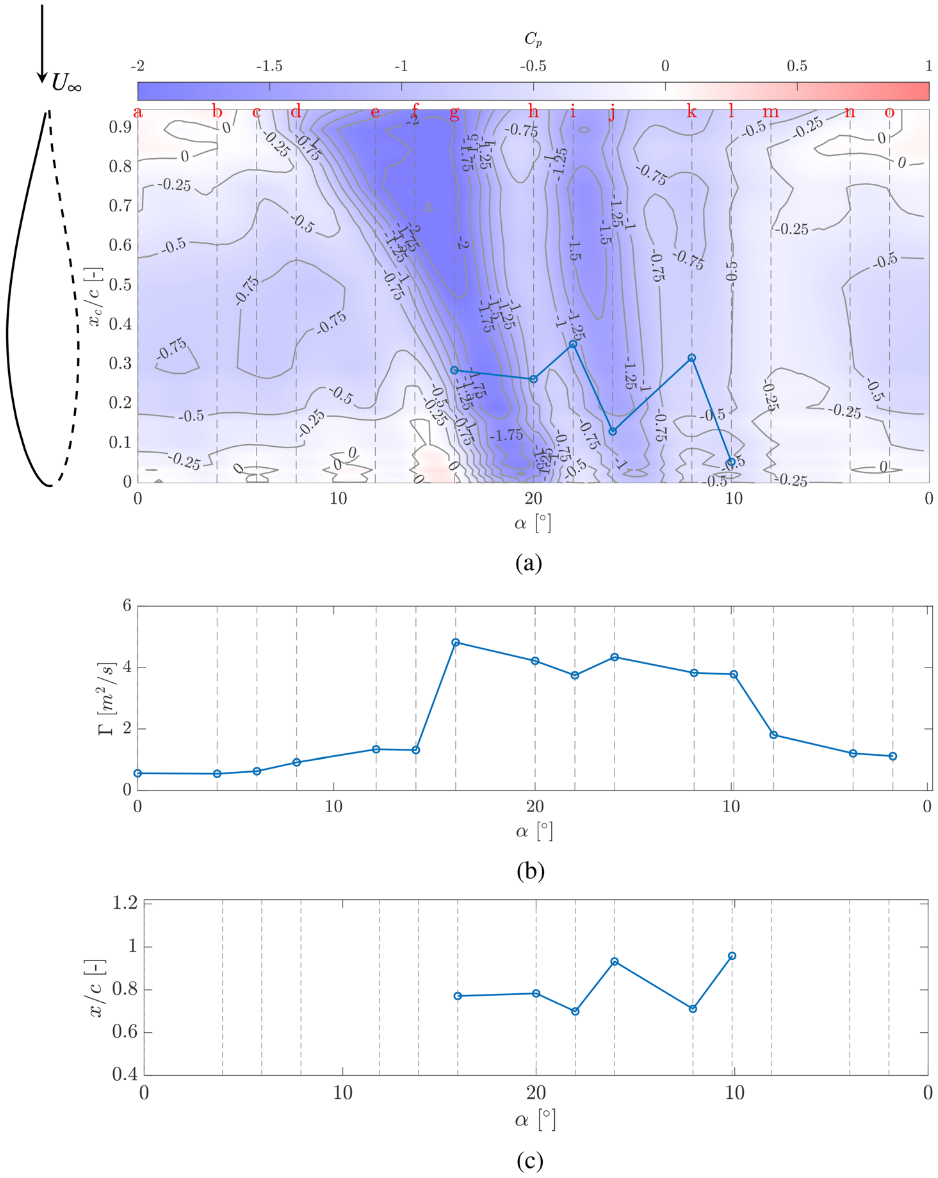

(a)

(b)

(c)

FIG. 6. Pressure and DSV information at case $\overline{\alpha}10\Delta10k0.1$: $\overline{\alpha}=10°$, $\Delta\alpha=10°$, and $k=0.1$. (a) Cycle-averaged pressure coefficient C_p on the suction surface over a pitching cycle. The vertical dashed lines represent measured PIV phases. The blue curve indicates the DSV core location in the chordwise direction, identified using the Γ_1 method.[30,31] (b) Circulation of the DSV at the measured PIV phases. (c) Streamwise location of the DSV core.

shows that Γ is initially relatively low until phase *f* and then increases sharply to a local maximum at phase *g*. It is noted that from phases *a* to *g*, the FoV of the PIV measurements is large enough to cover almost the full area of the vortex evolution; instead, from phase *h* onward, part of the vorticity from the DSV and TEV exits the field of view, yielding an under-estimation of Γ. At the same time, the C_p colormap indicates that during this upstroke period, the suction region (C_p below zero, blue areas) on the airfoil surface extends from less than 40% (phase *e*) to more than 90% (phase *g*) of the chord length.

Meanwhile, the pressure coefficient fields were derived from the PIV velocity measurements. The results are obtained by applying the Reynolds Averaged Navier–Stokes equation, and then solving for the static pressure using the Poisson equation formulation, as described by Van Oudheusden.[32] The boundary conditions adopted in the computations are specified as follows. At the inlet (left boundary of the PIV flow field), a Dirichlet boundary condition is imposed, with the pressure value determined from the Bernoulli equation. For the remaining boundaries, including the top, bottom, and right boundaries of the PIV flow field as well as the boundary of the airfoil, Neumann boundary conditions are applied, where the pressure gradients are obtained from the Navier–Stokes equations. The same boundary condition was applied previously by Xu *et al.*[33] As shown in Fig. 8, as the airfoil pitches up from phases *a* to *c* (aerodynamic leading edge moving down), a low-pressure region is present only on the airfoil suction (bottom) side, near the location of maximum thickness ($x_c/c \approx 0.4$). At phase *d*, the low-pressure region is concentrated at both the leading

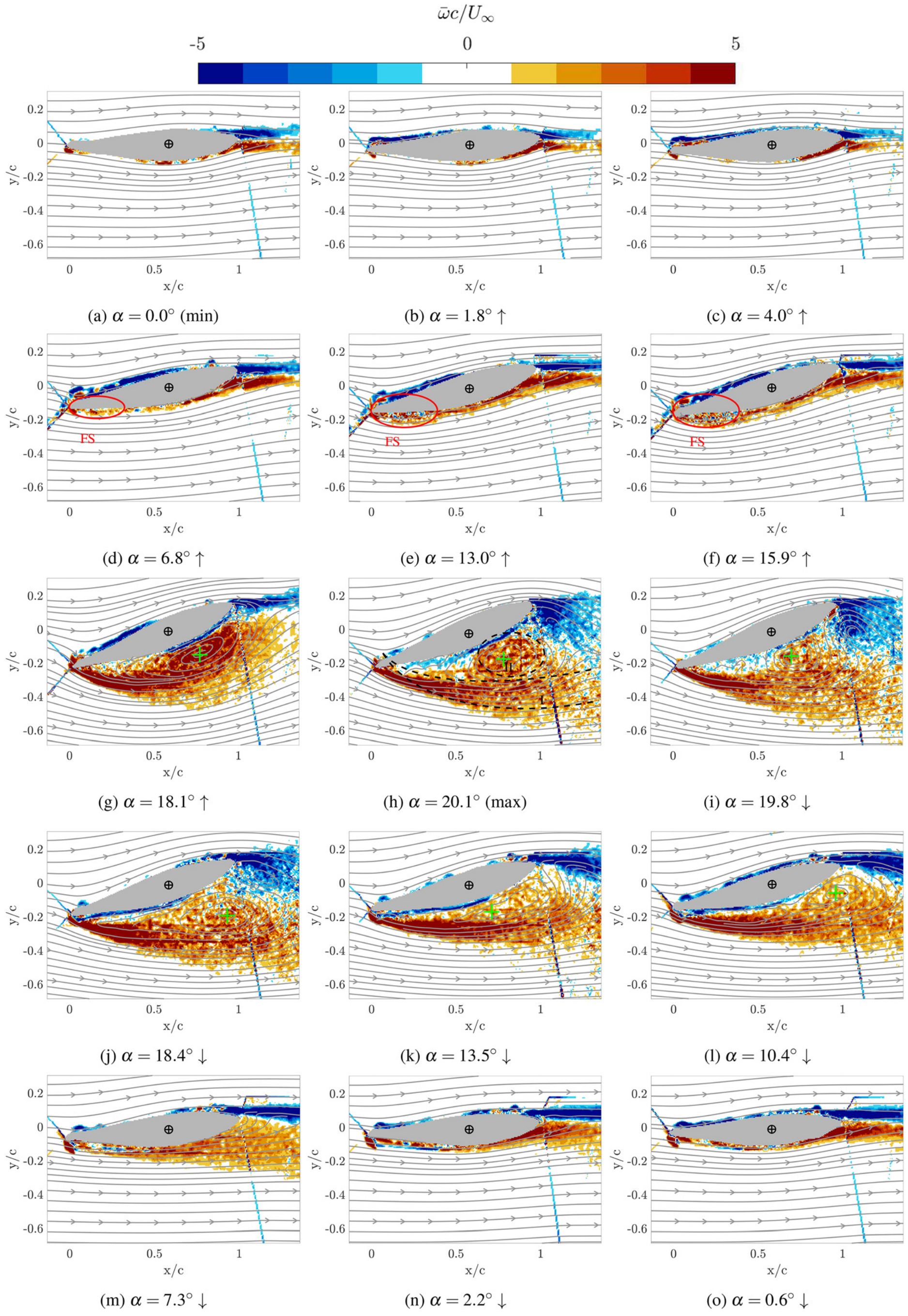

(a) $\alpha = 0.0°$ (min) (b) $\alpha = 1.8° \uparrow$ (c) $\alpha = 4.0° \uparrow$

(d) $\alpha = 6.8° \uparrow$ (e) $\alpha = 13.0° \uparrow$ (f) $\alpha = 15.9° \uparrow$

(g) $\alpha = 18.1° \uparrow$ (h) $\alpha = 20.1°$ (max) (i) $\alpha = 19.8° \downarrow$

(j) $\alpha = 18.4° \downarrow$ (k) $\alpha = 13.5° \downarrow$ (l) $\alpha = 10.4° \downarrow$

(m) $\alpha = 7.3° \downarrow$ (n) $\alpha = 2.2° \downarrow$ (o) $\alpha = 0.6° \downarrow$

FIG. 7. Vorticity field $\overline{\omega}c/U_\infty$ for case $\overline{\alpha}10\Delta10k0.1$: $\overline{\alpha} = 10°$, $\Delta\alpha = 10°$, $k = 0.1$. Green cross represents the location of DSV core center, identified using Γ_1 method.[30,31] FS: flow separation.

edge and the maximum thickness region. As the airfoil pitches up, higher suction takes place near the leading edge (phases *e* and *f*) and then the suction region grows bigger and reaches the maximum at phase *g*, where it covers the entire suction side of the airfoil, with the minimum C_p approaching -2. For higher angles of attack (phases *h* and *i*), the low-pressure region moves to the aerodynamic trailing edge, indicating the shedding of the DSV. Hence, it can be concluded that, during reverse flow dynamic stall, the DSV development follows a characteristic pressure propagation: first the leading edge experiences high suction, then (at $\alpha \approx 18°$) the suction region extends to the entire suction side of the airfoil, and finally (at $\alpha \approx 20°$) the vortex is shed downstream, resulting in the lower pressure near the aerodynamic trailing edge. This DSV-induced pressure fluctuation is widely recognized as the most dominant feature of dynamic stall and can be found in many

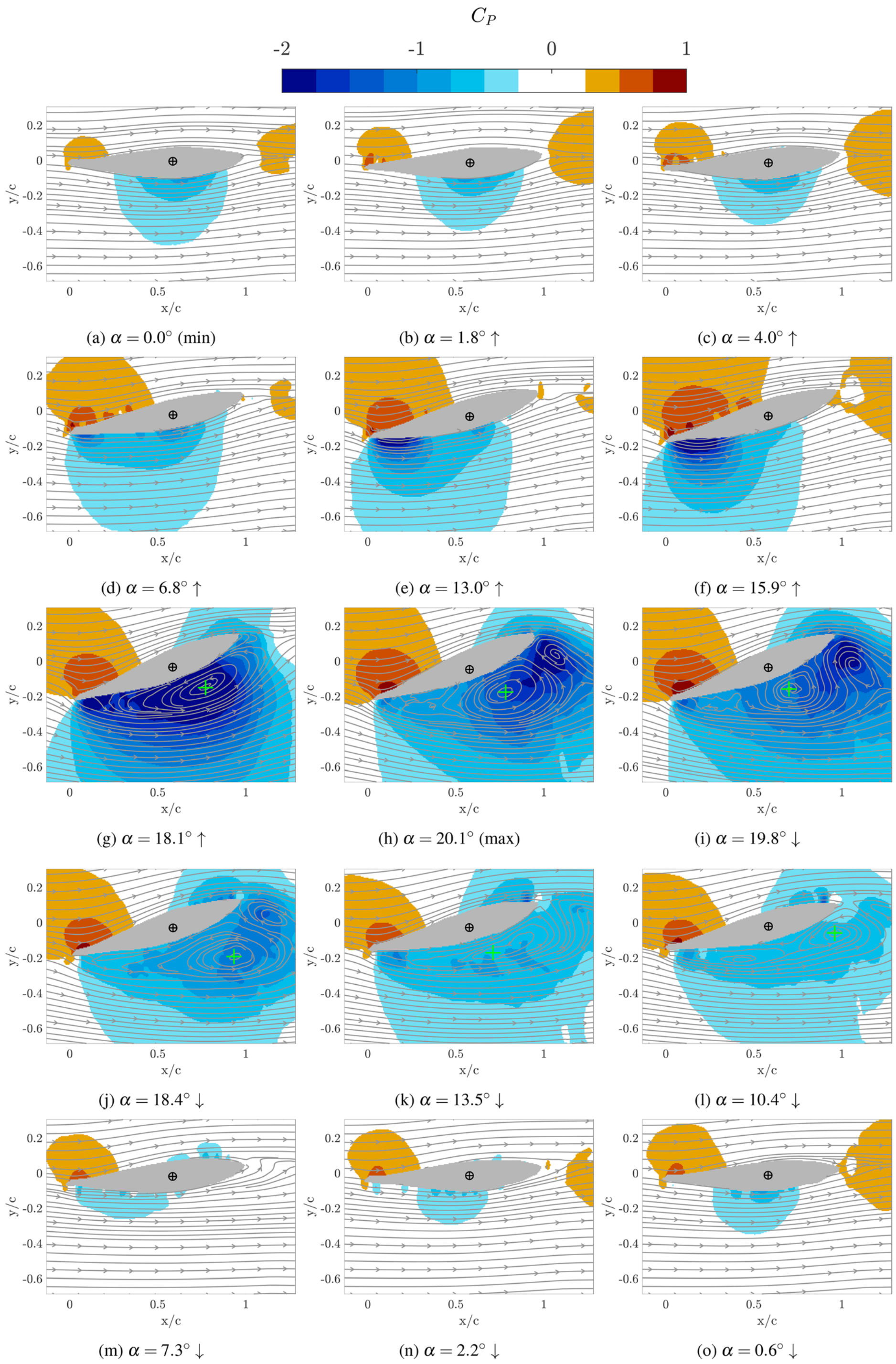

(a) $\alpha = 0.0°$ (min) (b) $\alpha = 1.8° \uparrow$ (c) $\alpha = 4.0° \uparrow$

(d) $\alpha = 6.8° \uparrow$ (e) $\alpha = 13.0° \uparrow$ (f) $\alpha = 15.9° \uparrow$

(g) $\alpha = 18.1° \uparrow$ (h) $\alpha = 20.1°$ (max) (i) $\alpha = 19.8° \downarrow$

(j) $\alpha = 18.4° \downarrow$ (k) $\alpha = 13.5° \downarrow$ (l) $\alpha = 10.4° \downarrow$

(m) $\alpha = 7.3° \downarrow$ (n) $\alpha = 2.2° \downarrow$ (o) $\alpha = 0.6° \downarrow$

FIG. 8. Pressure coefficient field C_p for case $\overline{\alpha}10\Delta10k0.1$ derived from PIV measured velocity field.

works in the literature[11,34,35] for conventional dynamic stall. Similarly, for reverse flow cases, Datta *et al.*[13] and Potsdam *et al.*[14] also documented the reverse flow DSV-induced pressure wave for helicopters. A comparison of the DSV-induced pressure wave from conventional and reverse flow dynamic stall will be discussed later in this section.

Successively, when the airfoil pitches up to the largest α of 20.1° [phase h, Fig. 7(h)], it is observed that the negative vorticity at the trailing edge increases (larger blue area). At phase g, the local circulatory flow shows signs of TEV formation. This TEV is induced by the upstroke motion and the convection of the DSV toward the trailing edge, which both lead to the increase in adverse pressure gradient near the trailing edge. When the airfoil pitches to the maximum angle at phase *h*, the TEV grows bigger, which causes a higher suction near the trailing edge region. At the same time, from phases *g* to *h*, the DSV partially separates from the airfoil surface [marked by region I in Fig. 7(h)]. Meanwhile, the inner part of the DSV remains attached to the airfoil, which is marked by region II in Fig. 7(h). Overall, this partial separation leads to a decrease in Γ within the FoV [Fig. 6(b)]. After reaching the maximum α, the airfoil starts to pitch down (aerodynamic trailing edge moving down) and the vorticity field is shown from phase *i* [Fig. 7(i)] to phase *o* [Fig. 7(o)]. As α decreases to 19.8° [phase *i*, Fig. 7(i)], the TEV grows larger. Together with the downstroke movement of the airfoil, the recirculating part of the DSV moves upstream, as shown in Fig. 6(c) from $x/c = 0.78$ (phase *h*) to $x/c = 0.69$ (phase *i*). Due to the upstream motion of the DSV during this period, the negative C_p region at phase *i* expands toward the upstream location, while for the previous phase (*h*), the negative C_p region concentrates at the trailing edge region, which can be seen in Fig. 6(a). Following the partial separation phases of *h* and *i*, at phase *j* [Fig. 7(j)], the attached DSV grows, fed by the shear layer separating at the aerodynamic leading edge. This growth is facilitated by the TEV shedding, which allows the DSV to develop unimpeded. This leads to an increase in circulation measured inside the FoV. As the airfoil continues pitching down to approximately 7.3° (phase *m*), the DSV moves away from the trailing edge, and the flow begins to reattach onto the airfoil surface progressively. During this period, the circulation within the FoV drops sharply and returns to a value close to zero by the end of the cycle.

The aerodynamic force and moment during the pitching process for this case are also examined. The results are obtained through the integration from the measured pressure. The hysteresis loops of the lift coefficient C_l and pitching moment coefficient C_m are shown in Fig. 9. Solid lines indicate the upstroke motion, while the dashed lines represent the downstroke motion. These two lines represent the cycle averaged value, while the red shaded area (very thin in the plot) represents the 95% confidence interval level. The measured PIV phases are also marked on the lines. As the airfoil pitches up from phase *a* to phase *c*, the flow remains attached; thus, both C_l and C_m vary approximately linearly with the angle of attack. From phase *c* to phase *g*, C_l keeps decreasing, owing to the increasing suction from the growing DSV. In this period from phase *c* to phase *f*, as the airfoil pitches up, the DSV-induced suction at the leading edge generated ahead of the pitching axis [as shown in Figs. 8(d)–8(f)] creates a counterclockwise (negative) moment on the airfoil. At the same time, the suction near the trailing edge only has a minor impact on generating the clockwise (positive) moment. Thus from phase *c* to phase *f*, C_m decreases. At phase *g*, the DSV causes the huge suction region over 90% of the airfoil length from the leading edge [see Fig. 6(a)]. This suction, centered on the downstream (right-hand) side of the airfoil pitching axis, creates a clockwise (positive) moment. This is the reason for the increase in C_m at phase *g*. Meanwhile, at phase *g*, C_l reaches the maximum absolute value while the DSV is still attached and features maximum strength. Between phases *g* and *h*, the partial detachment of the DSV leads to a drop in C_l. Between these two phases, C_m also decreases due to the decrease in suction on the airfoil surface. Afterward, as the airfoil pitches up (phases *h* to phase *j*), both C_l and C_m first feature an increase in magnitude due to the higher suction induced by the attached (partial) DSV (phases *h* and *i*) and then (phases *i* and *j*) a decrease in magnitude as the DSV convects away from the airfoil. As the airfoil pitches further down from phase *j* to phase *o* until the end of the downstroke cycle, the DSV convects further away from the trailing edge, and C_l and C_m decrease in magnitude. Overall, the hysteresis loops indicate two times the sharp increase in C_l and C_m magnitude, which are related to the DSV initial growth (phases *d* to *g*) and the attached DSV moving upstream (phases *h* and *i*), respectively. The second increase in C_l and C_m is smaller compared to the first one, as (1) the strength of the attached DSV is smaller compared to the original DSV, (2) the second increase happens during the downstroke period, therefore the DSV decreases in strength when α returns back to 0.

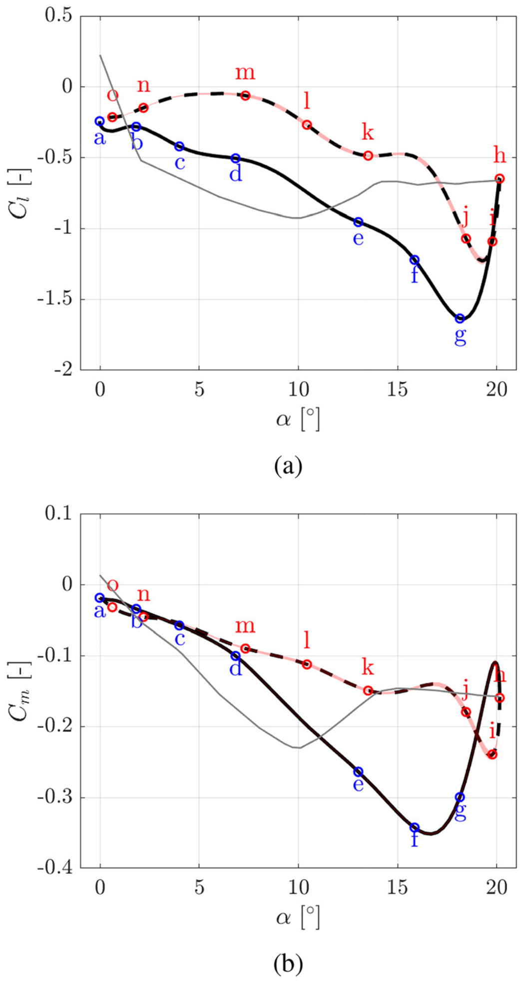

FIG. 9. Hysteresis loop of the lift coefficient C_l, and pitching moment coefficient C_m for case $\overline{\alpha}10\Delta10k0.1$. Line styles and confidence intervals as described in the text. PIV phases are marked on the curves.

The static C_l measurement is marked as the gray line in Fig. 9(a). During the range of the pitching angles from 0° to 20° (α' from 180° to 160°), C_l decreases to the minimum of -0.93 at 10.1°. Afterward, the C_l magnitude decreases due to flow separation. After 14.2°, the steady C_l curve remains relatively constant at approximately -0.67. The C_p distributions on the airfoil surface from 10° to 20° are shown in Fig. 10(a). The suction side is represented as a solid line and the pressure side as a dashed line. Initially from 10° to 13°, the suction side has a C_p peak region near the aerodynamic leading edge ($x_c/c = 1$, which is the geometric trailing edge), which is ascribed to the flow separation near the sharp leading edge. From 14° to 20°, the flow on the suction side remains fully separated, with only minor changes near the trailing edge ($x_c/c = 0$) for the pressure side. This leads to the stable C_l after 14.2°.

Compared to the steady C_l, during pitching [Fig. 9(a)], the upstroke motion leads to a higher magnitude and a delayed magnitude drop near phase *g*. Similarly, compared to the static C_m [the gray curve in Fig. 9(b)], dynamic C_m presented at this pitching case also shows a lower minimum from approximately -0.22 (static) to -0.35 (dynamic) and a delayed magnitude recovery. This aligns with conventional dynamic stall results, where a lift and moment overshoot is reported.[3,5] Meanwhile, it is also shown that for α between 1.2° and 12.6°, both upstroke and downstroke motions lead to a lower C_l magnitude compared to the static case. The C_p distributions compared to the steady C_l at 10° are shown in Fig. 10(b). For the steady measurement, the suction side is marked as the black solid line, and the pressure side is marked as the black dashed line. For the pitching cases, lines of C_p distribution when $|\alpha - 10| \leq 0.2$ are plotted. The pressure side C_p remains close to the steady case, with the main differences lying in the suction side C_p. During the downstroke motion, the flow remains fully separated from the airfoil surface, which creates the low flat C_p on the suction side. This uniform C_p is also shown in Fig. 6(a) (marked by line *o*) and C_p map [Fig. 8(l)]. These results contribute to a lower C_l compared to the steady measurement during the downstroke period. During the upstroke period, strong suction regions are observed near the leading edge and around the pitching axis location ($x_c/c = 0.4$), as evidenced in Figs. 8(d) and 8(e). The lower $-C_p$ magnitude outside these regions leads to the deviation from the suction side of the steady result, leading to an overall decrease in C_l values.

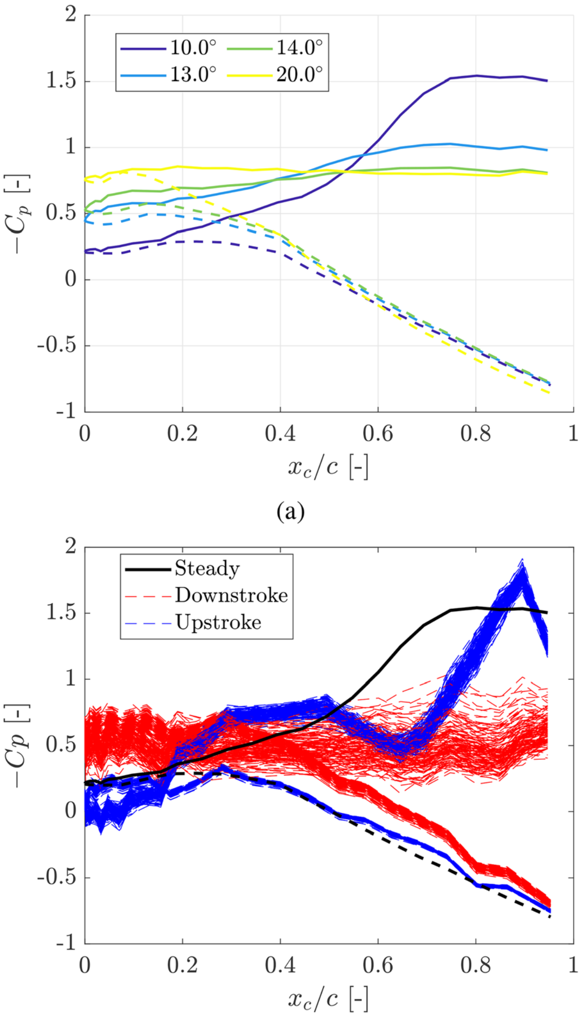

(a)

(b)

FIG. 10. C_p distribution (a) from 10° to 20° for steady measurement (solid lines represent suction side and dashed lines represent pressure side) and (b) at 10° for both the steady and unsteady cases.

Through the examination of all DSV-present cases, suction side C_p in a reverse flow condition shows distinct patterns where multiple suction regions can be found. Appendix C (Fig. 31) reports the results for representative tested cases. In order to compare the difference between conventional and reverse flow dynamic stall, a conventional dynamic stall case tested in this campaign is shown in Fig. 11, where $\overline{\alpha'} = 10^\circ$, $k = 0.16$, and $\Delta\alpha = 10^\circ$. The phases measured by PIV are marked by vertical dashed lines, and the corresponding vorticity fields are shown in Fig. 33 in Appendix E. Note that the colormap and colorbar range are modified in order to match the result as shown in Visbal and Benton.[34] In their research, large eddy simulation was performed on a NACA 0012 airfoil at angles of attack ramped up from a minimum value of $\alpha' = 4^\circ$ to a maximum of $\alpha' = 30^\circ$.[36] During the upstroke period, the conventional test case in this campaign shows similar patterns to the reverse-flow case. However, the leading edge is characterized by extremely low pressure ($C_p < -5$) between approximately $\alpha' = 10^\circ$ to a maximum of $\alpha' = 20^\circ$. This extremely low pressure is ascribed to the development and burst of the laminar separation bubble (LSB).[36]

For this conventional (non-reverse) flow case, the C_p distribution on the airfoil surface at $\alpha' = 18^\circ$ (phase *f* for the upstroke) is shown in Fig. 12. The unsteady cases are plotted for $|\alpha' - 18| \leq 0.2$. The result shows that at phase *f* (the red curves), C_p from the suction side exceeds the value from the steady measurement. Especially at the leading edge region (between $x_c/c = 0.002$ and 0.03), the C_p overshoot leads to a plateau near $-C_p = 5.3$, which indicates the presence of a leading edge separation bubble. From the PIV vorticity field, it is shown that from phase *d* [Fig. 33(d)] to phase *f* [Fig. 33(f)], the flow separation occurs near the trailing edge of the airfoil's suction side. From phase *g* [Fig. 33(g)] to phase *i* [Fig. 33(i)], the trailing edge separation leads to the roll-up of the shear layer and eventually to the formation of the DSV at phase *i*. Therefore, for conventional cases, the LSB at the leading edge plays an important role, which creates abrupt pressure drops prior to the DSV development. Similar spatial–temporal suction side C_p pattern can be found in many previous works in the literature.[11,34,35] In contrast, reverse flow conditions exhibit a more gradual pressure decrease during the initial DSV formation period, as consistently observed across all DSV-present cases (representative cases shown in Appendix C, Fig. 31). In forward flow, the streamlined

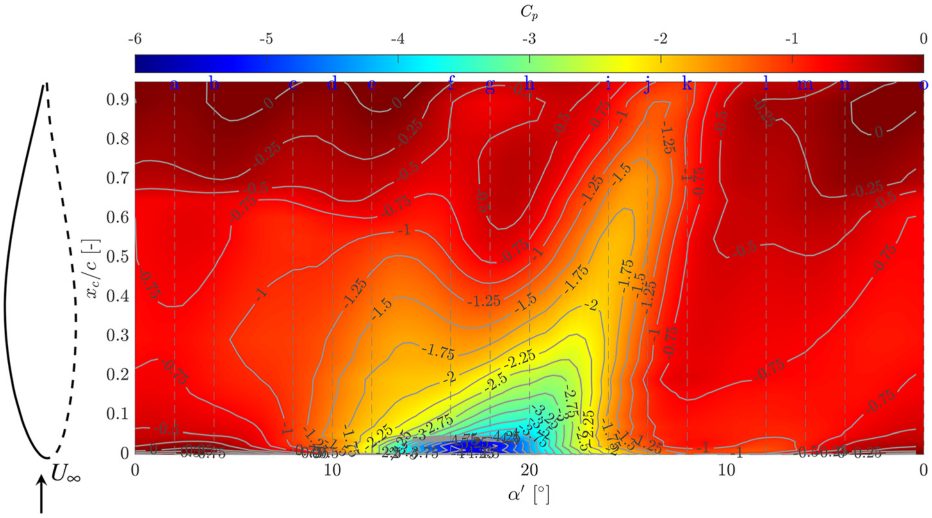

FIG. 11. Cycle-averaged pressure coefficient C_p on the suction surface at case $\overline{\alpha}'10\Delta10k0.16$. The PIV measured phases are marked by vertical dashed lines and the vorticity fields of which are shown in Fig. 34.

leading edge accelerates the flow smoothly, creating a suction peak just downstream of $x_c/c \approx 0.002$, followed by a deceleration. In reverse flow, the sharp leading edge triggers immediate separation even at a small angle of attack, resulting in a flat, low-pressure plateau ($-C_p \approx 1.5$) in the separated flow region (Fig. 10). This lack of acceleration/deceleration contrasts sharply with the C_p dynamics of forward flow.

Overall, during one pitching cycle of case $\overline{\alpha}10\Delta10k0.1$, a single DSV is shed at the end of the downstroke, while partial flow separation occurs once during the upstroke due to the increasing angle of attack. This experimental observation captures the detailed vortex evolution throughout the pitching cycle in a reverse flow dynamic stall scenario. It suggests that the DSV shedding process is influenced by the interactions with the shear layer emanating from the sharp leading edge, which continues to feed into the still-attached portion of the DSV. In comparison, Hodara *et al.*[37] observed two DSVs in one pitching cycle during their reverse flow dynamic stall experiments using a NACA 0012 airfoil at $\overline{\alpha} = -8.9°$, $\Delta\alpha = 9.9°$, $Re = 3.3 \times 10^5$, and $k = 0.16$. Their C_p maps indicated two distinct suction regions, and instantaneous PIV images showed that the second DSV formed during the downstroke. Notably, the vortices in their study were fully separated, in contrast to the partially attached vortices observed in the present work. Such partially attached vortices are not only linked to additional force fluctuations but also influence flow reattachment dynamics and the unsteady aerodynamic loading. Additionally, in conventional dynamic stall cases, the dynamic stall development typically involves an initial instability stage followed by the formation of a DSV,[10] which differs from the behavior observed under reverse flow conditions. The present research provides a detailed physical understanding of the DSV development mechanism in reverse flow, showing that (1) the flow separation at the initial stage of DSV development leads to a gradual C_p decrease compared to the conventional dynamic stall case, where the LSBs lead to a suction peak before the DSV forms. (2) Moreover, the partial DSV attachment and the shear layers feeding of the attached DSV lead to additional force fluctuations during the pitching cycle.

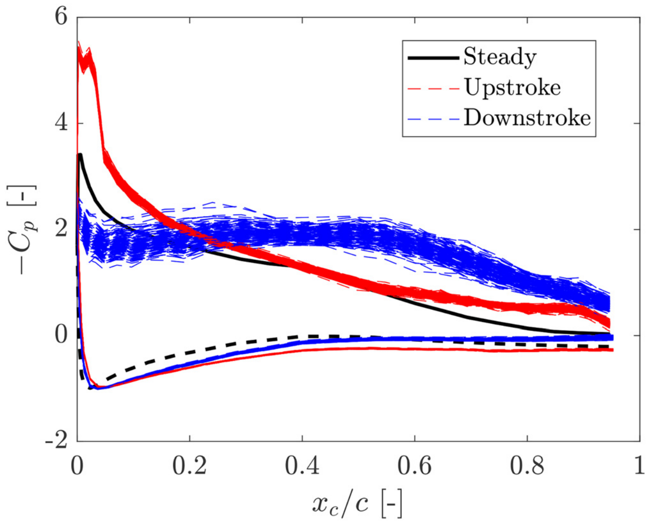

FIG. 12. C_p distribution at 18° for both the steady and unsteady cases for the conventional dynamic stall case $\overline{\alpha}'10\Delta10k0.16$.

2. Extended suction region case: $\overline{\alpha}20\Delta10k0.1$

This section discusses the flow physics of case $\overline{\alpha}20\Delta10k0.1$, where only the mean pitching angle is changed to 20° compared to the previous case (case $\overline{\alpha}10\Delta10k0.1$). The suction side C_p and DSV evolution are shown in Fig. 13, the PIV vorticity fields are shown in Fig. 14, and C_p obtained from the PIV flow field are present in Fig. 32.

Two major differences in pressure imprint can be found between these two cases. First, the suction region persists over a significantly larger portion of the pitching cycle in case $\overline{\alpha}20\Delta10k0.1$ compared to $\overline{\alpha}10\Delta10k0.1$. While the lower angle case ($\overline{\alpha}10\Delta10k0.1$) exhibits the maximum suction near mid-cycle (phase *g*, corresponding to $\alpha = 18.1°$), the higher angle case ($\overline{\alpha}20\Delta10k0.1$) develops suction immediately at the minimum pitch angle of 10°, maintaining it

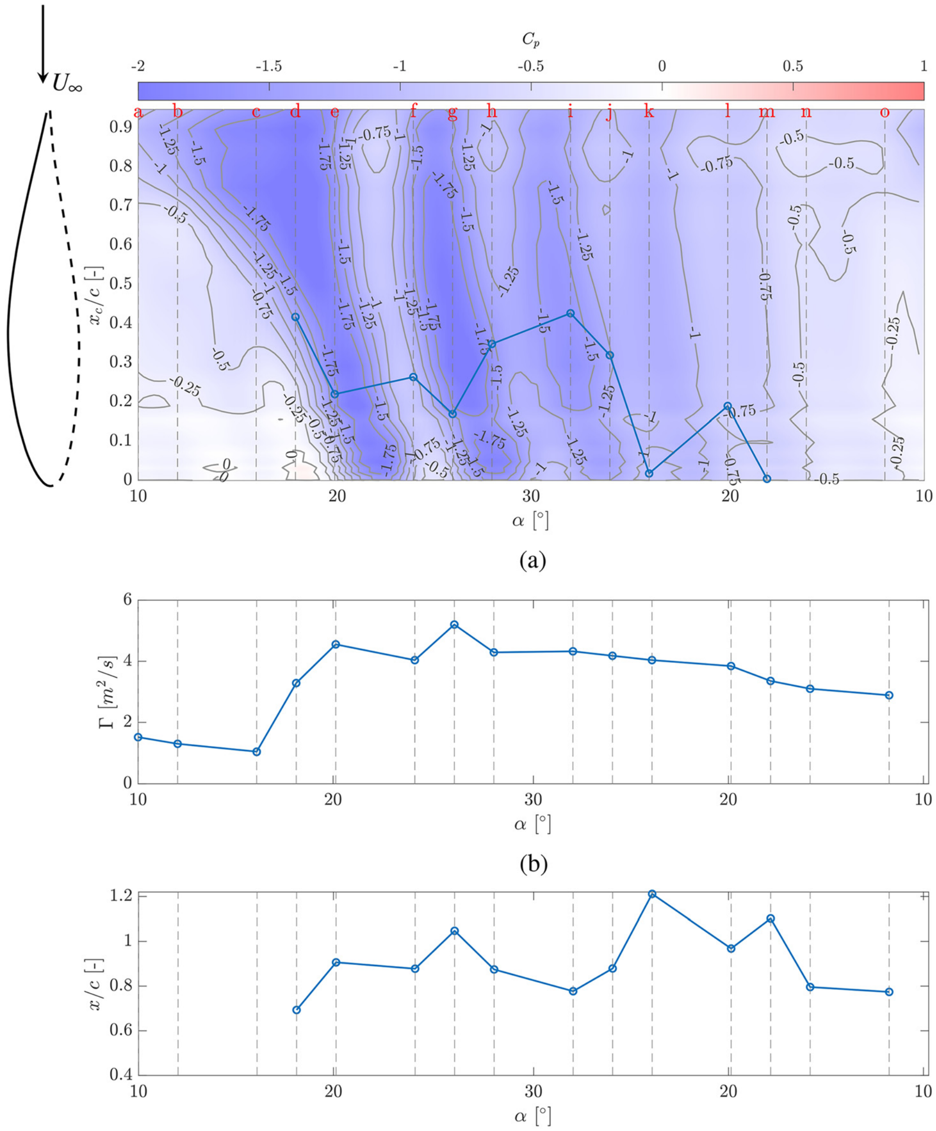

(a)

(b)

(c)

FIG. 13. Pressure and DSV information at case $\overline{\alpha}10\Delta10k0.1$: $\overline{\alpha}=10^\circ$, $\Delta\alpha=10^\circ$, and $k=0.1$. (a) Cycle-averaged pressure coefficient C_p on the suction surface over a pitching cycle. The vertical dashed lines represent measured PIV phases. The blue curve indicates the DSV core location in the chordwise direction, identified using the Γ_1 method.[30,31] (b) Circulation of the DSV at the measured PIV phases. (c) Streamwise location of the DSV core.

throughout the motion. Examples can be seen from phases *a* [Figs. 14(a) and 32(a)] and *b* [Figs. 14(b) and 32(b)], where the leading edge flow separation is present at both phases, yielding a suction pressure growth at the beginning of the upstroke cycle. It is also noticed from phase *o*, the last captured downstroke phase, that the shear layer emanating from the aerodynamic leading edge is still detached from the airfoil surface [Fig. 14(o)], which indicates that the growth of the DSV starts from the previous cycle at the end of the downstroke period. Overall, this wider suction region on the airfoil surface is inherent for case $\overline{\alpha}20\Delta10k0.1$ as it has a higher α during pitching. As a result, C_l and C_m for case $\overline{\alpha}20\Delta10k0.1$ (Fig. 15) already feature large variations with the angle of attack near the small α region (from phases *o* to *a* to *b*).

Second, unlike case $\overline{\alpha}10\Delta10k0.1$, where the partial separation of the DSV happens once, the C_p map of case $\overline{\alpha}20\Delta10k0.1$ shows three major enclosed suction areas on the airfoil suction side, which are linked to the multiple partially separated DSV. Initially, from phase *a* [Fig. 14(a)] to phase *d* [Fig. 14(d)], the DSV starts forming from the leading edge, becoming fully visible at phase *d*. During this period, the DSV remains attached to the airfoil surface; Γ is initially low up to phase *c*, and then it increases at phase *d* due to the vorticity feeding from the shear layer. As the airfoil pitches up from phase *d* to phase *e* [Fig. 14(e)] and *f* [Fig. 14(f)], the DSV starts to detach from the airfoil surface. Similar to case $\overline{\alpha}10\Delta10k0.1$, the DSV is partially shed, marked by the region I in Fig. 14(e), while the inner part remains attached to the airfoil surface (marked by region II). Different from case $\overline{\alpha}10\Delta10k0.1$, this interaction happens during the early stage of the upstroke period, which is attributed to the higher α for this case.

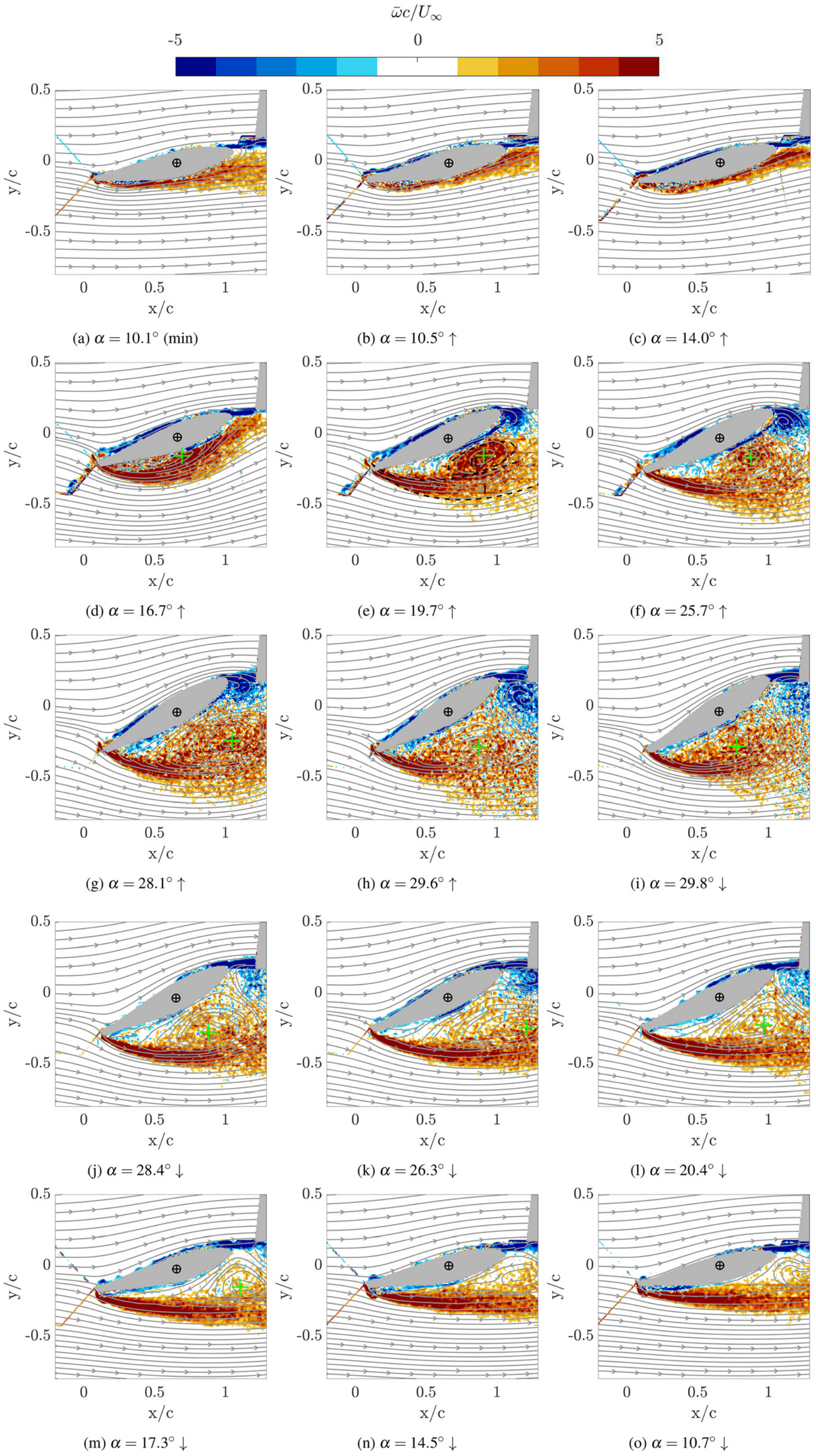

(a) $\alpha = 10.1°$ (min) (b) $\alpha = 10.5° \uparrow$ (c) $\alpha = 14.0° \uparrow$

(d) $\alpha = 16.7° \uparrow$ (e) $\alpha = 19.7° \uparrow$ (f) $\alpha = 25.7° \uparrow$

(g) $\alpha = 28.1° \uparrow$ (h) $\alpha = 29.6° \uparrow$ (i) $\alpha = 29.8° \downarrow$

(j) $\alpha = 28.4° \downarrow$ (k) $\alpha = 26.3° \downarrow$ (l) $\alpha = 20.4° \downarrow$

(m) $\alpha = 17.3° \downarrow$ (n) $\alpha = 14.5° \downarrow$ (o) $\alpha = 10.7° \downarrow$

FIG. 14. Vorticity field $\overline{\varpi}c/U_\infty$ for case $\overline{\alpha}20\Delta10k0.1$: $\overline{\alpha} = 20°$, $\Delta\alpha = 10°$, $k = 0.1$. Green cross represents the location of DSV core center, identified using Γ_1 method.[30,31]

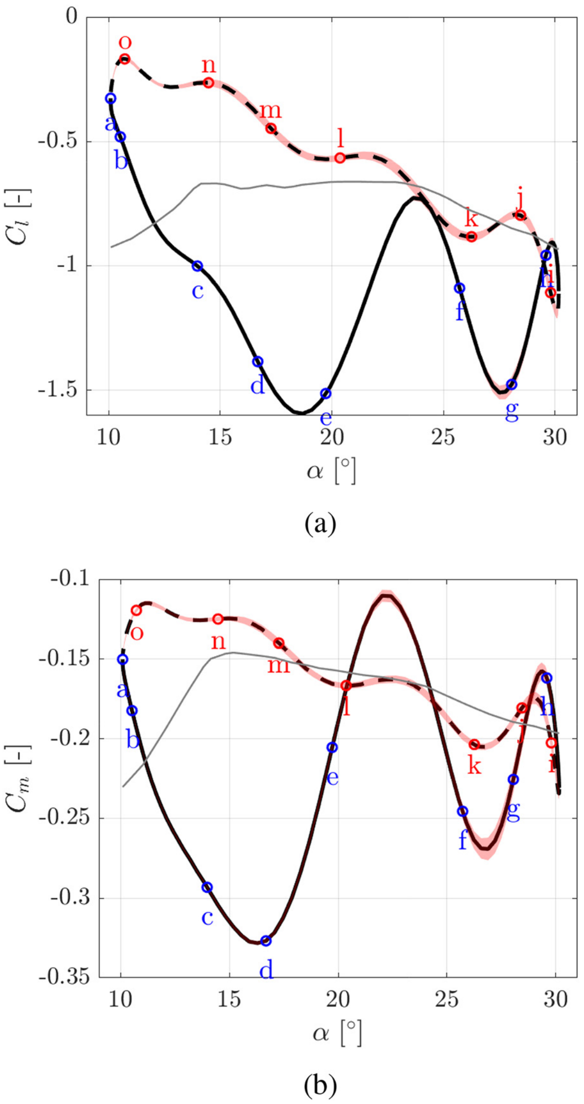

(a)

(b)

FIG. 15. Hysteresis loop of the lift coefficient C_l, and pitching moment coefficient C_m for case $\overline{\alpha}10\Delta10k0.1$. Line styles and confidence intervals as described in the text. PIV phases are marked on the curves.

Similarly, from phase *g* to phase *h*, from phase *i* to phase *j*, and from phase *k* to phase *l*, the same partial separation can be observed: at the earlier phase of the two (phase *g*, *i* or *k*), the C_p distribution on the suction surface [Fig. 13(a)] reaches the local minimum, with the vorticity field featuring a round-contour DSV, which is attached to the airfoil surface; At the latter phase (phase *h*, *j* or *l*), the shear layer does not fully recirculate back toward the surface; instead, its outer part sheds into the wake. Owing to this, phases *e*, *g*, *i*, and *k* lie roughly near the local peak of C_l, and the C_l recovery happens at the corresponding following phases, as shown in Fig. 15(a).

Apart from the hysteresis of C_l, the hysteresis of C_m also exhibits similar characteristics compared to case $\overline{\alpha}10\Delta10k0.1$, where the location of the DSV highly influences the variation of the C_m value. For example, during the initial DSV formation period, the low pressure region starts from the leading edge (phase *a*, [Figs. 14(a) and 32(a)] and then extends to close to the pitching axis [Figs. 14(d) and 32(d)]. As a result, it creates a counterclockwise moment, which leads to the decrease in C_m. After the DSV development in phase *d*, at phase *e* [Figs. 14(e) and 32(e)], the partially attached DSV is located on the right-hand side of the pitching axis, generating a clockwise motion, which increases C_m.

Therefore, compared to the single partial separation observed in case $\overline{\alpha}10\Delta10k0.1$, case $\overline{\alpha}20\Delta10k0.1$ presents four partial separations, which is a more complex flow dynamics due to the higher pitching angles. Although previous research on conventional dynamic stall also focused on the development of the DSV,[10,38,39] the influence of the partial separation was not discussed. Our experimental campaign reveals that the partial separation leads to the secondary growth of the DSV, which can happen multiple times during the pitching cycle, depending on different pitching parameters (as shown in Fig. 31). This partial separation extends the overall DSV development time and delays the time at which the DSV detaches. In addition, the DSV vortex formation leads to an increased magnitude of the aerodynamic lift, followed by a reduction when partial DSV separation occurs; as indicated before, this process occurs multiple times (specifically for case $\overline{\alpha}20\Delta10k0.1$, four times) during the oscillation cycle.

B. POD analysis

As established, dynamic stall under reverse flow conditions presents a complex aerodynamic phenomenon marked by multiple (partial) separations and shedding of the DSV. Building on previous POD analyses of conventional dynamic stall,[9,17,40] we employ Proper Orthogonal Decomposition (POD) of the pressure coefficient *Cp* on the suction side of the airfoil, across all cases where a DSV is present, to identify the dominant flow features characterizing the reverse flow conditions. The energy contents from the first two POD modes are shown in Table III, clearly indicating that the first two modes together contribute to about 90% of the total energy. The results are grouped by $\overline{\alpha}$. For cases with $\overline{\alpha} = 5°$, a single dominant mode captures more than of 76% of the total energy, suggesting that the flow is highly dominated by one distinct flow pattern. For the other cases with $\overline{\alpha} = 10°, 15°$, and 20°, the first mode decreases its dominance, with the lowest value 46.9% of the total energy. This indicates that for larger $\overline{\alpha}$, two prominent flow patterns coexist, suggesting a more complex flow dynamics compared to the single-mode dominance observed at lower angles. The different flow regimes are color-coded, which will be explained at the end of this section.

To investigate the spatial location of these high-energy activities, the mode shapes ϕ of the first mode for all the cases are shown in Fig. 16, where each sub-figure contains the result from the cases with the same $\overline{\alpha}$. Since POD mode shapes are determined up to an arbitrary sign, we analyze their absolute peak values to identify the most dominant flow features.

For $\overline{\alpha} = 5°$ and 10° cases [Figs. 16(a) and 16(b)], the first mode shapes exhibit uniform peaks near the aerodynamic leading edge ($x_c/c = 1$), indicating that the most dominant modes are concentrated in this region. This peak in the mode shape is likely associated with the dynamics, namely, formation and growth, of the DSV. Conversely, for $\overline{\alpha} = 15°$, the mode shapes become less monotonic; in general, two local maxima are present, one at the leading edge and

TABLE III. Energy distribution of the most dominant mode(s) across all cases, grouped by $\overline{\alpha}$. The flow regimes are color-coded as follows: orange for DSV-dominated flow, black for TEV-dominated flow, and blue for mixed-energy cases where both vortices contribute significantly. The classification criteria for these regimes are discussed later in this section.

Case	E_1 (%)	E_2 (%)
$\overline{\alpha}5\Delta10k0.05$	84.6	8.9
$\overline{\alpha}5\Delta10k0.08$	84.4	9.2
$\overline{\alpha}5\Delta10k0.1$	85.6	8.1
$\overline{\alpha}5\Delta10k0.13$	87.7	6.5
$\overline{\alpha}5\Delta10k0.16$	89.9	4.7
$\overline{\alpha}5\Delta10k0.18$	91.2	4.3
$\overline{\alpha}5\Delta15k0.05$	80.8	14.2
$\overline{\alpha}5\Delta15k0.1$	76.6	18.3
$\overline{\alpha}10\Delta5k0.05$	56.9	31.9
$\overline{\alpha}10\Delta5k0.1$	60.6	28.2
$\overline{\alpha}10\Delta5k0.16$	68.7	20.8
$\overline{\alpha}10\Delta5k0.21$	75.9	14.4
$\overline{\alpha}10\Delta10k0.05$	57.8	27.6
$\overline{\alpha}10\Delta10k0.08$	59.7	28.4
$\overline{\alpha}10\Delta10k0.1$	59.2	30.9
$\overline{\alpha}10\Delta10k0.13$	57.9	33.2
$\overline{\alpha}10\Delta10k0.16$	58.3	32.6
$\overline{\alpha}10\Delta10k0.18$	58.8	31.4
$\overline{\alpha}10\Delta15k0.05$	75.9	18.4
$\overline{\alpha}10\Delta15k0.1$	65.3	28.8
$\overline{\alpha}15\Delta5k0.05$	90.9	7.8
$\overline{\alpha}15\Delta5k0.1$	63.6	32.2
$\overline{\alpha}15\Delta5k0.16$	52.4	40.9
$\overline{\alpha}15\Delta5k0.21$	60.4	32.1
$\overline{\alpha}15\Delta10k0.05$	54.4	36.7
$\overline{\alpha}15\Delta10k0.08$	54.1	38.2
$\overline{\alpha}15\Delta10k0.1$	52.6	39.7
$\overline{\alpha}15\Delta10k0.13$	46.9	45.2
$\overline{\alpha}15\Delta10k0.16$	50.3	42.0
$\overline{\alpha}15\Delta10k0.18$	53.6	37.9
$\overline{\alpha}15\Delta15k0.05$	62.3	28.1
$\overline{\alpha}15\Delta15k0.1$	54.9	37.9
$\overline{\alpha}20\Delta10k0.05$	69.7	26.9
$\overline{\alpha}20\Delta10k0.08$	57.6	38.1
$\overline{\alpha}20\Delta10k0.1$	58.4	35.9
$\overline{\alpha}20\Delta10k0.13$	54.8	39.1
$\overline{\alpha}20\Delta10k0.16$	55.8	38.2
$\overline{\alpha}20\Delta10k0.18$	57.5	35.8
$\overline{\alpha}20\Delta15k0.05$	67.7	26.4
$\overline{\alpha}20\Delta15k0.1$	54.2	39.1
$\overline{\alpha}20\Delta15k0.16$	51.0	40.8
$\overline{\alpha}25\Delta10k0.18$	75.7	21.0
$\overline{\alpha}25\Delta15k0.05$	71.7	25.5
$\overline{\alpha}25\Delta15k0.1$	60.6	33.9
$\overline{\alpha}25\Delta15k0.16$	55.1	38.2

one at the trailing edge, respectively. For example, for the case $\overline{\alpha}15\Delta10k0.1$ [the red curve in Fig. 16(c)], the mode shape is relatively flat, with the value of -0.24 at $x_c/c = 0.69$ and -0.25 at $x_c/c = 0.19$. This means that, in such a case, the flow contains equally significant energy at the leading edge and trailing edge, which suggests that the DSV and the TEV contribute equally to the flow dynamics. When $\overline{\alpha} = 20°$ and $25°$, even though some cases still shows a mixture of energy from both the leading edge and the trailing edge, the other cases (including $\overline{\alpha}20\Delta10k0.1$, $\overline{\alpha}20\Delta10k0.13$, $\overline{\alpha}20\Delta15k0.05$, $\overline{\alpha}20\Delta15k0.1$, $\overline{\alpha}25\Delta10k0.18$, $\overline{\alpha}25\Delta15k0.05$, and $\overline{\alpha}25\Delta15k0.1$) start to exhibit dominance from the trailing edge only. This result suggests that, at higher mean angles of attack, the flow is dominated by the dynamics of the TEV.

To validate the assumption that links mode shapes to vortex dynamics, the rest of this section analyzes examples of DSV-dominated and TEV-dominated flows using POD.

1. DSV-dominated flow

As a representative case, we consider case $\overline{\alpha}10\Delta10k0.1$, where the most dominant mode exhibits a pronounced peak in the leading edge region. The first two mode shapes (ϕ_1 and ϕ_2) and the time average C_p (ϕ_0) at each chordwise location are shown in Fig. 17. The temporal coefficient of the first two modes, along with the cycle-averaged Cp variation at chordwise location $x_c/c = 0.05$ and 0.95, are presented in Fig. 18. These two locations are chosen since they are the peak locations of ϕ_1 and ϕ_2.

Overall, ϕ_0 experiences a decreasing trend from the trailing edge to the leading edge, which is representative of a large flow separation occurring from the leading edge and covering most of the suction side of the airfoil. While ϕ_1 exhibits a peak near the leading edge ($x_c/c = 1$), ascribed to the formation and growth of the DSV, ϕ_2 has a local peak near the trailing edge region, which is attributed to the TEV dynamics. From the perspective of the temporal coefficient (Fig. 18), mode 1's temporal coefficient exhibits an increasing trend during the upstroke cycle; during this period, the formation of the DSV leads to an increasing leading edge suction. Consequently, the first peak of mode 1's temporal coefficient coincides with the suction peak of C_p near the leading edge ($x_c/c = 0.9$). Similarly, the second peak of mode 1's temporal coefficient coincides with the suction peak at the same chordwise location during the downstroke period; this suction peak is due to the secondary development of the attached DSV. Likewise, for the second mode, the temporal coefficient starts to increase when C_p at $x_c/c = 0.05$ starts to decrease near $\alpha = 17°$ during upstroke. The two peaks in mode 2's temporal coefficient align with the two C_p suction peaks at $x_c/c = 0.05$. As a result, the first mode correlates with the dynamics of the DSV. Similarly, the temporal-spatial correspondence strongly indicates that mode 2 physically represents the dynamics of TEV development during dynamic stall.

In order to further investigate the physical meaning of each mode, C_p is reconstructed based on the first two modes. The results are shown in Fig. 19 with chordwise distribution in the left column and spatial-temporal field in the right column. ϕ_1 (times a constant h) is added/subtracted to/from the mean C_p (ϕ_0); the result is shown in Fig. 19(a). By adding (or subtracting) ϕ_1, the mean C_p shows decreasing (or increasing) values separately. The variation is the highest close to the leading edge ($x_c/c > 0.6$), and gradually diminishes closer to the trailing edge; when $x_c/c < 0.2$, the variation is the minimum.

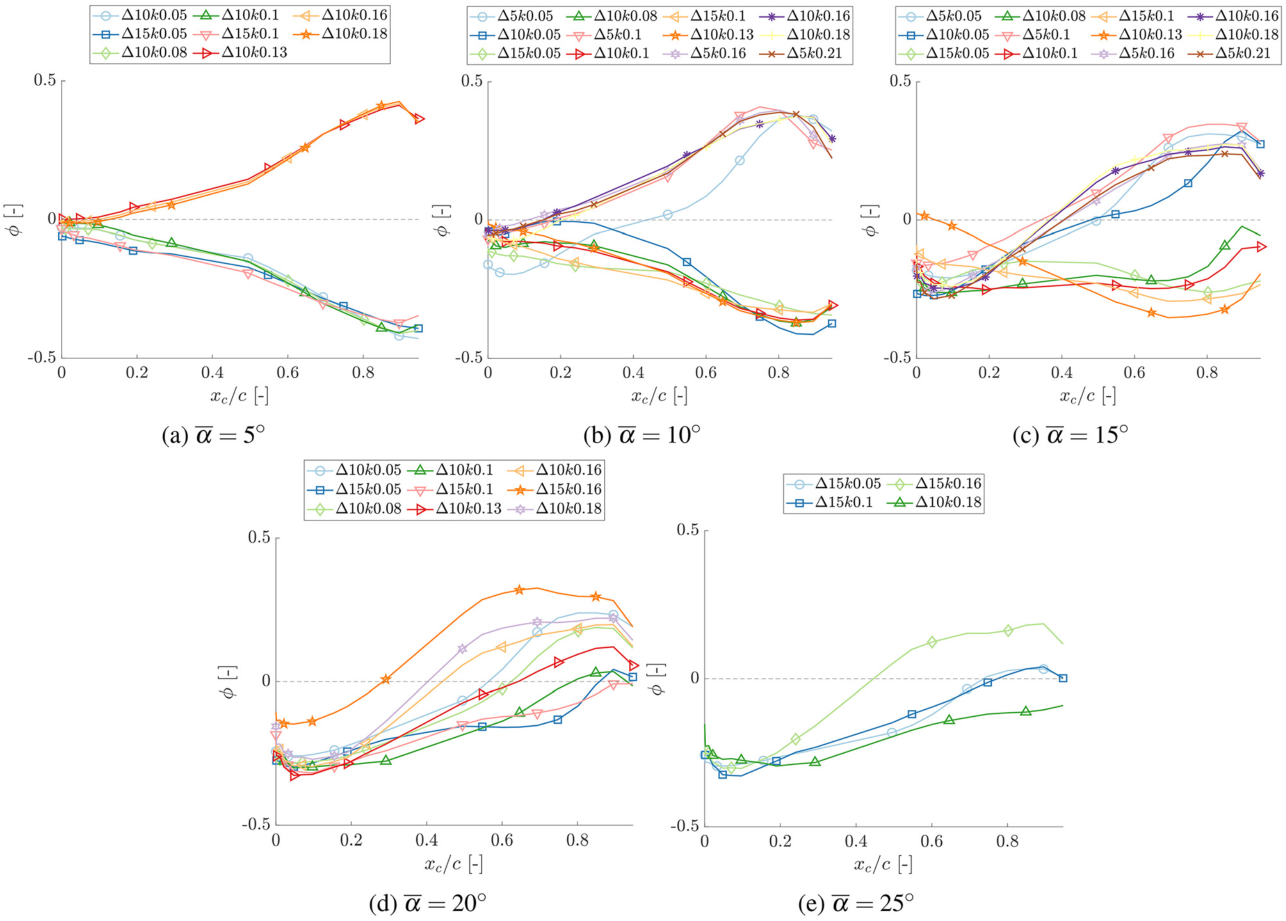

(a) $\overline{\alpha} = 5°$ (b) $\overline{\alpha} = 10°$ (c) $\overline{\alpha} = 15°$

(d) $\overline{\alpha} = 20°$ (e) $\overline{\alpha} = 25°$

FIG. 16. POD mode shapes of the most dominant mode (mode 1) for each case.

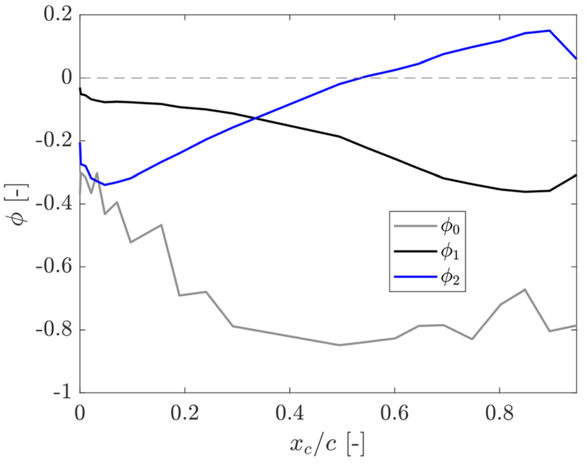

FIG. 17. POD mode shapes of the time averaged C_p (ϕ_0) and the first two modes (ϕ_1 and ϕ_2) at case $\overline{\alpha}10\Delta10k0.1$.

Meanwhile, the spatial-temporal C_p reconstructed from mode 1 [Fig. 19(b)] presents two suction regions near the leading edge, which correspond to the DSV and the secondary development of the DSV, respectively. Based on the reconstructed C_p, it can be concluded that mode 1 is correlated with the growth and decay of the DSV.

The reconstructed C_p from mode 2 is shown in Figs. 19(c) and 19(d). Contrary to mode 1, by adding (or subtracting) this mode, C_p shows decreasing (or increasing) values, stemming from the middle of the airfoil ($x_c/c = 0.5$) toward the trailing edge ($x_c/c = 0$). At the same time, C_p in the leading edge region increases or decreases, opposite to the variation in the trailing edge region. The spatial–temporal plot [Fig. 19(d)] shows that the reconstructed C_p from mode 2 creates two trailing edge suction areas, which are correlated with the TEV development. Meanwhile, a high-pressure region is present near the leading edge at the same phases, which increases the leading edge pressure in mode 2. Therefore, mode 2 is related to two physical activities: first, it is highly correlated with the growth and decay of the trailing edge vortex. Second, as a minor effect, it is also related to the growth (or the pressure recovery) of the DSV, as a consequence of the decay (or growth) of the TEV.

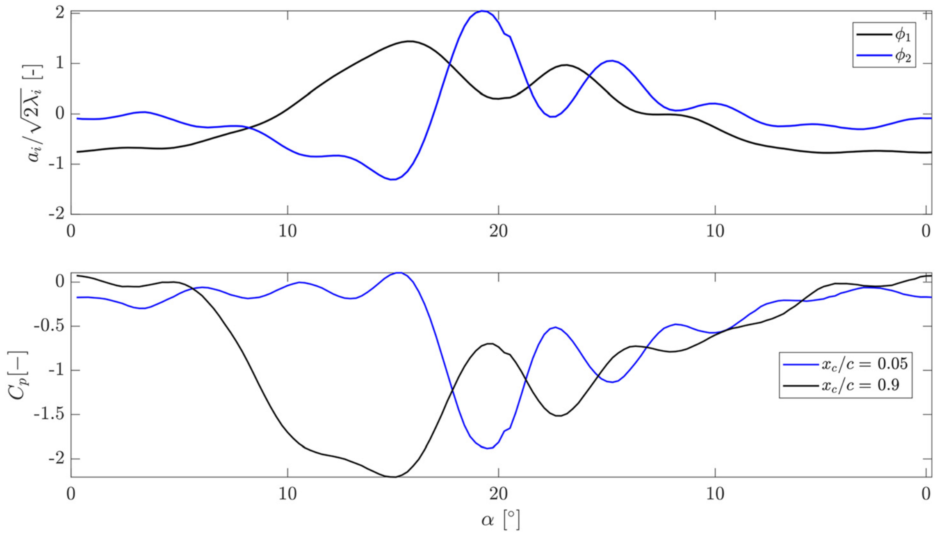

FIG. 18. Temporal coefficient of the first two dominant modes (top) and suction side C_p (bottom) at case $\overline{\alpha}10\Delta10k0.1$.

2. TEV-dominated flow

The case $\overline{\alpha}20\Delta10k0.1$ is selected as representative of TEV-dominated flow dynamics. The dominating mode shapes are shown in Fig. 20, with the mean C_p also shown for comparison. Compared to the previous case, the mean C_p distribution presents lower values, with $C_p < -0.5$ even at the trailing edge, indicating a large flow separation affecting the entire suction side of the airfoil. As already discussed, in this case, the first mode peaks near the trailing edge region, opposite to $\overline{\alpha}10\Delta10k0.1$, and the second mode has a wider peak region on the airfoil center region, but still peaks at approximately 30% from the leading edge.

The temporal coefficient of the first two modes, together with the phased-averaged suction side C_p at $x_c/c = 0.05$, 0.69, 0.6, 0.8, and 0.9, are shown in Fig. 21. The two chordwise locations at $x_c/c = 0.05$ and 0.69 correspond to the mode shape peaks as shown in Fig. 20. The other locations at $x_c/c = 0.6$, 0.8, and 0.9 are plotted to explain the reason why the first mode shape peaks at $x_c/c = 0.69$, which will be discussed later. The variations of C_p and the temporal coefficient are related to multiple DSV separations and sheddings, as discussed in the previous section. It is observed in Fig. 21 that the first mode starts to increase sharply when C_p at $x_c/c = 0.05$ starts to decrease near $\alpha = 17°$ during upstroke. When C_p reaches the local minimum at $x_c/c = 0.05$, mode 1 reaches the local peak values simultaneously. This means that mode 1 is correlated with the development of the TEV. The reconstructed C_p from mode 1 is shown in Figs. 22(a) and 22(b) for its chordwise distribution and spatial-temporal distribution, respectively. By adding (or subtracting) ϕ_1, the C_p distribution decreases (or increases) accordingly, with the largest variations occurring in the trailing edge region ($x_c/c = 0.02$ to 0.5), and almost no variation in the leading edge region (from $x_c/c = 0.75$ and onward). The reconstructed C_p from this mode shows a concentration of suction areas near the trailing edge region, extending up to approximately $x_c/c = 0.75$. The multiple suction regions are associated with the dynamics of the DSV, and in particular, its formation and the subsequent secondary effect from the partially attached DSVs. The large value of mode 1 in the trailing edge region and the high correlation between its temporal coefficient and the pressure coefficient near the trailing edge allow us to conclude that mode 1 is related to the growth and decay of the TEV. By comparing the vorticity field from the two cases (Figs. 7 and 14), it is shown that, in the latter case, the TEV is formed much earlier during the upstroke period and its size is much bigger, which indicates its stronger impact on the overall flow dynamics.

Instead, mode 2 presents (negative) peaks when C_p at $x_c/c = 0.69$ reaches the local minimum, indicating that this mode represents the dynamics of the energy from $x_c/c = 0.69$ the most. In order to examine the physical meaning of this mode, the reconstructed C_p chordwise distribution and space-temporal distribution are shown in Figs. 22(c) and 22(d). This mode presents the maximum C_p fluctuation from the leading edge ($x_c/c = 1$) up until $x_c/c = 0.19$. No major fluctuation is seen near the trailing edge region by adding or subtracting the normalized ϕ_2. In the spatial-temporal field, it is shown that the suction areas are located near the leading edge, which indicates that mode 2 represents the growth and decay of the DSV. In the previous case ($\overline{\alpha}10\Delta10k0.1$, Mode 1), the highest energy concentrations associated with the DSV appear near the leading edge, indicating strong flow instability initiation there. However, in this case, the dominant energy peaks shift to a different region (closer to mid-chord at $x_c/c = 0.69$), suggesting a different DSV development pattern. From the temporal coefficient and C_p plot (Fig. 21), it is shown that the lowest C_p is obtained at the same time in the entire region from the leading edge ($x_c/c = 0.9$) until $x_c/c = 0.69$, at $\alpha_1 = 17.1°$ marked in the plot. Afterwards, due to the initiation of the TEV, the development of the DSV is hindered, which brings a later suction peak at $x_c/c = 0.6$ at $\alpha_2 = 17.5°$ marked in the plot. This also explains the high mode shape values of mode 2 between $x_c/c = 0.6$ toward the leading edge; at the moment the TEV starts to initiate, the DSV develops the most, and the temporal coefficient of mode 2 reaches the highest value.

C. Trend from POD analysis for reverse flow dynamic stall

Overall, the two cases presented above showcase two different flow regimes, which are either DSV-dominated or TEV-dominated. In

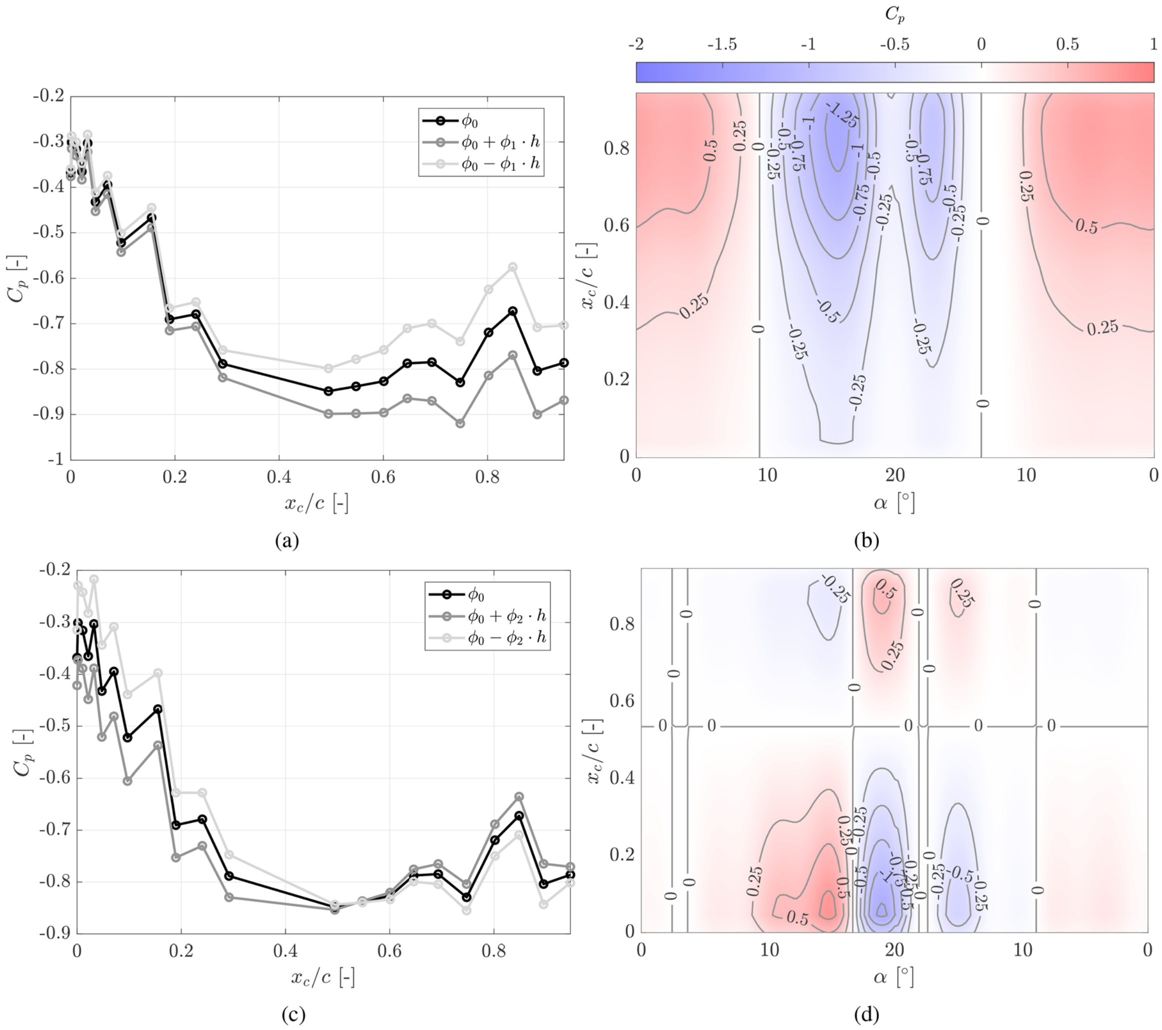

FIG. 19. Reconstructed C_p chordwise distribution (left column) and reconstructed C_p spatial–temporal field (right column) from the first mode (the first row) and the second mode (the second row) for case $\overline{\alpha}10\Delta10k0.1$.

order to investigate the flow regimes for all the test cases in Table III, the following procedure is followed:

1. A reconstruction of the suction side C_p field is performed based on the first mode, similar to what is shown in Figs. 19 and 22.
2. If the reconstruction field represents the dynamics from only the DSV or the TEV (i.e., the C_p increases or decreases centered at the leading edge or trailing edge region),
   - If $E_1 - E_2 \geq 25\%$, then the first mode is the most dominant mode and represents one single dominant dynamics from the DSV or the TEV. These two flow regimes are marked by orange and black separately.
   - If $E_1 - E_2 < 25\%$, then the first two modes are both considered important in the flow. Then, an additional reconstruction of C_p is performed based on the second mode. For all the relevant cases, the second mode represents the dynamics of the TEV or the DSV, respectively. Therefore, these cases are classified as a mixed type of energy, marked by blue.
3. If the reconstruction field represents the dynamics from both the DSV and the TEV, these cases are also classified as mixed energy type (blue).

The classification of the flow regimes is shown in Table III. Overall, the trend is clear: at low mean angles of 5° and 10°, the flow is DSV dominated, where the growth and decay of the DSV determine the majority of the force variation. When the mean angle increases to 15°, the DSV loses its dominance, and the flow starts to show a mixture of energy from both the DSV and the TEV. When the mean angle increases to 20° and 25°, although a mixture of energy is still present, more cases are dominated by the dynamics of the TEV. These results indicate that, across the studied reduced frequency range (k from 0.05 to 0.21) and pitching amplitude range ($\Delta\alpha$ from 5° to 15°), $\overline{\alpha}$ emerges

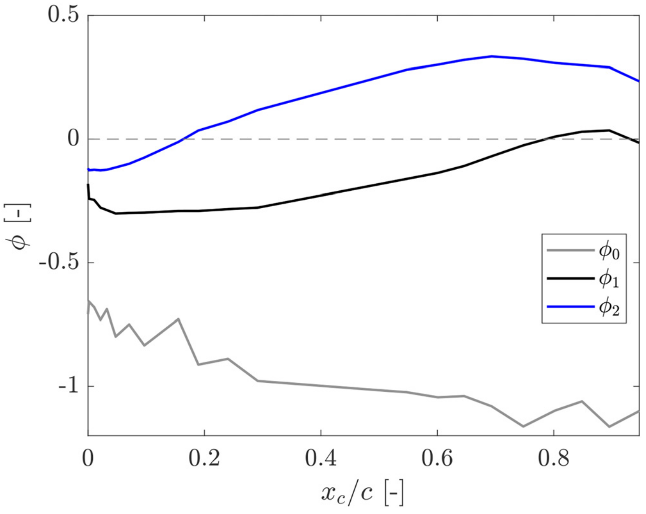

FIG. 20. POD mode shapes of the time averaged C_p (ϕ_0) and the first two modes (ϕ_1 and ϕ_2) at case $\overline{\alpha}20\Delta10k0.1$.

as the governing parameter for determining dominant flow regimes identified through POD analysis. For $\overline{\alpha} = 5°$, the low mean angle results in suction-side C_p distributions (Appendix C, Fig. 31) that lack a distinct suction peak near the trailing edge, indicating underdeveloped TEV. As the mean angle increases to $\overline{\alpha} = 10°$, while the dominant mode still captures the DSV dynamics [Fig. 16(b)], the second mode gains substantially more energy (minimum 14.4%), which primarily reflects the growing influence from the TEV on the flow structure. However, for higher mean angles of 15°, 20°, and 25°, multiple separation and shedding events disrupt the DSV development. Together with the initiation of competing TEV structures, they lead to a mixture of both DSV and TEV energy or even a TEV-only-dominant flow regime.

Despite this $\overline{\alpha}$-dependent trend, within the cases with the same $\overline{\alpha}$ of 15°, 20°, and 25°, variations can be found. For example, at $\overline{\alpha} = 20°$ and $\Delta\alpha = 10°$, both $k = 0.1$ and 0.13 cases exhibit TEV-dominated flow [Fig. 16(b)], while the remaining four cases ($k = 0.05$, 0.08, 0.16, and 0.18) are dominated by both DSV and TEV. The C_l hystereses of these cases are plotted in Fig. 23. All cases present negative peak(s) during the upstroke period (solid lines). As discussed in the previous section, the decrease in C_l during the upstroke is due to the formation of the DSV, while the increase in C_l is due to its partial detachment from the airfoil's surface. As the reduced frequency increases, C_l reaches its peak at a later time (or angle) during the upstroke period, which causes an enlargement in the hysteresis loop. This trend with k aligns with previous literature with conventional dynamic stall cases.[4,15]

In cases $\overline{\alpha}20\Delta10k0.05$ and $\overline{\alpha}20\Delta10k0.08$, the upstroke period presents peaks with smaller amplitudes compared to the remaining four cases. The spatial–temporal evolution of C_p for these two cases, as shown in Figs. 31(h) and 31(i), presents underdeveloped DSV and TEV. Therefore, the dominant energy for these two cases comes from a mixture of both DSV and TEV. It is also interesting to note that even at the lowest frequency ($k = 0.05$), which is considered as a quasi-steady condition,[16] the unsteady loop differs from the steady curve. This indicates that the transition between quasi-steady and unsteady behavior in reverse flow dynamic stall may occur at frequencies lower than $k = 0.05$, where the discrepancy between steady and unsteady responses becomes minimal. On the contrary, cases $\overline{\alpha}20\Delta10k0.1$ and $\overline{\alpha}20\Delta10k0.13$ each present two negative peaks in the hysteresis loop, both with larger amplitudes. The spatial–temporal C_p of these two cases [Figs. 31(j) and 31(k)] exhibits two DSV-induced suction regions during the upstroke period, which indicates multiple separations during upstroke. Furthermore, these cases feature fully developed TEVs. Consequently, the DSV dynamics are suppressed by both the DSV intermittent separation and the strong TEV influence, resulting in TEV-dominated flow characteristics for these conditions.

At higher reduced frequencies (cases $\overline{\alpha}20\Delta10k0.16$ and $\overline{\alpha}20\Delta10k0.18$), the hysteresis loops exhibit a single dominant peak

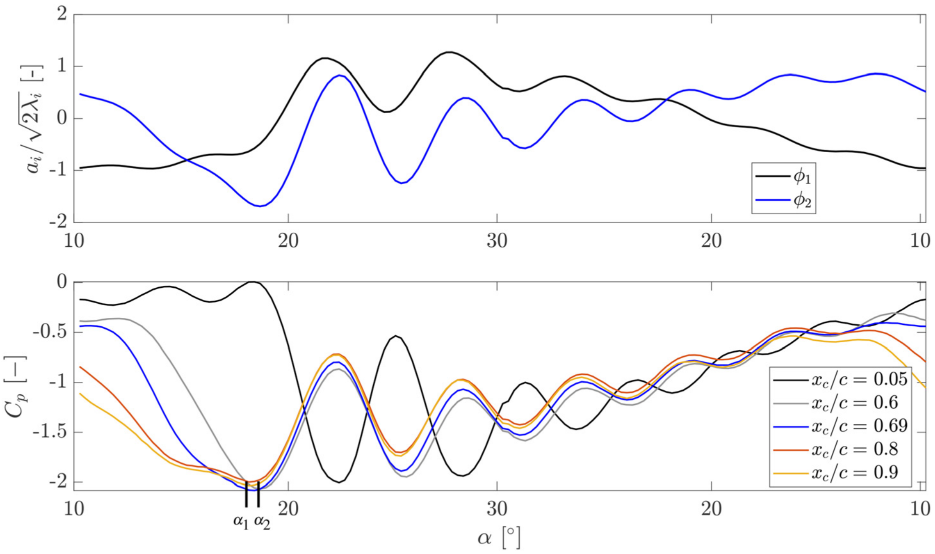

FIG. 21. Temporal coefficient of the first two dominant modes (top) and suction side C_p (bottom) at case $\overline{\alpha}20\Delta10k0.1$. α_1 is the angle where the suction peak occurs between $x_c/c = 0.9$ and $x_c/c = 0.69$. α_2 is the angle where the suction peak occurs at $x_c/c = 0.6$.

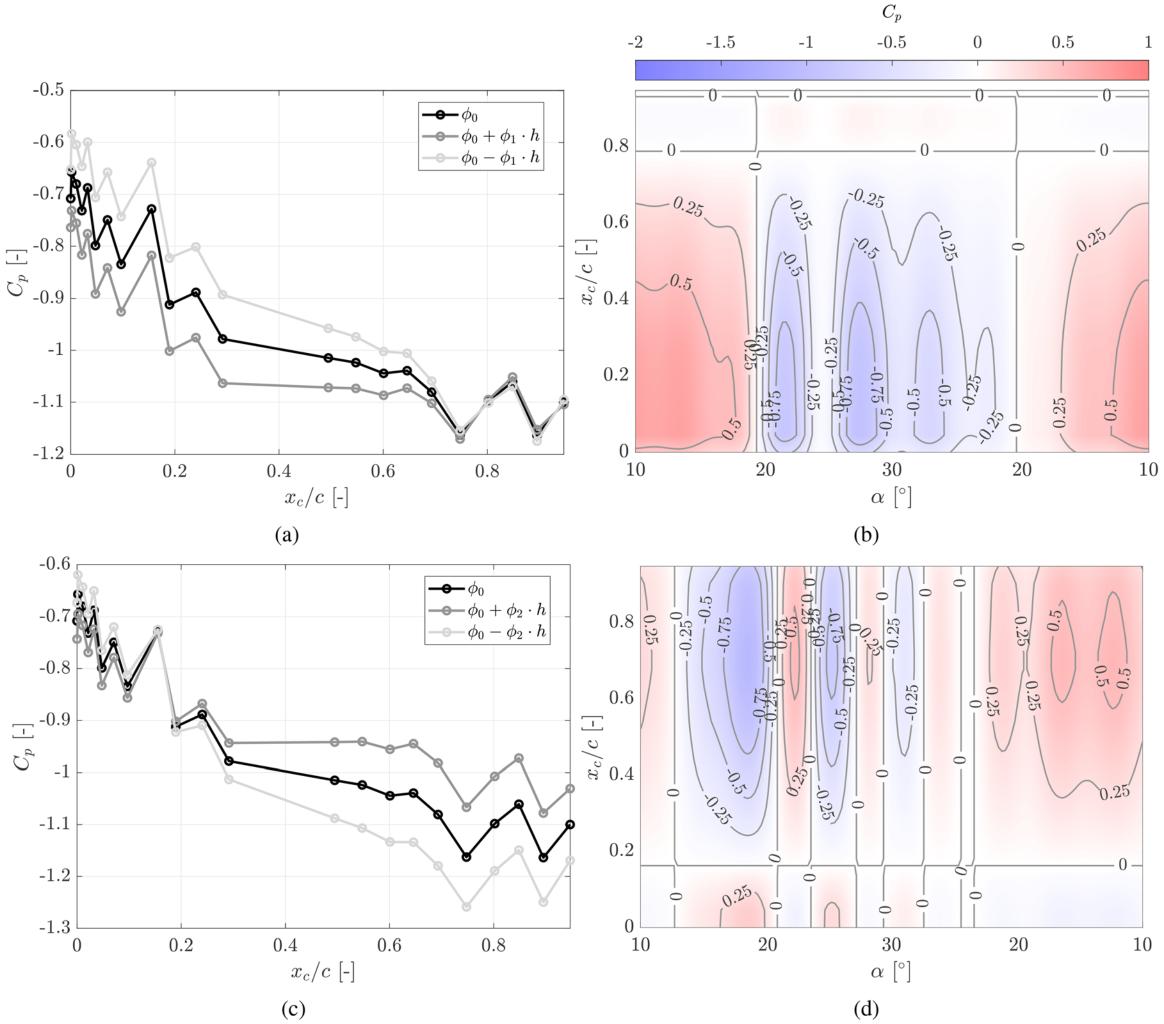

(a) (b)

(c) (d)

FIG. 22. Reconstructed C_p chordwise distribution (left column) and reconstructed C_p spatial–temporal field (right column) from the first mode (the first row) and the second mode (the second row) for case $\overline{\alpha}20\Delta10k0.1$.

during the upstroke. The corresponding spatiotemporal C_p distributions [Figs. 31(l) and 31(m)] reveal an extensive DSV-induced suction region persisting throughout the upstroke. Simultaneously, the TEV development generates comparable suction levels (average $C_p = -2.5$). The competing energy contributions from both vortices result in a mixed flow regime.

Therefore, at a mean angle of $\overline{\alpha} = 20°$ and $\Delta\alpha = 10°$, the dominant flow regime is characterized by contributions from both the DSV and TEV, depending on k. For low values of k, both vortices are underdeveloped, while high k values lead to strong, competing DSV and TEV structures. In both cases, the resulting flow reflects a mixture of energies from the two vortices. In contrast, at intermediate k, multiple DSV separations occur, leading to a flow regime dominated by the TEV. Similarly, at both $\overline{\alpha}20\Delta15k0.16$ [Fig. 31(p)] and $\overline{\alpha}25\Delta15k0.16$ [Fig. 31(t)] cases, the flow reflects a comparable mixture of energies, arising from the competition between the DSV and TEV.

It is important to note that the influence of k on the flow behavior is not universal but case-dependent. For instance, the case $\overline{\alpha}15\Delta5k0.1$ exhibits a DSV-dominated flow, in contrast to the other three cases with the same mean angle and amplitude ($\overline{\alpha}15\Delta5k0.05$, $\overline{\alpha}15\Delta5k0.16$, and $\overline{\alpha}15\Delta5k0.21$), which all display a mixed vortex regime. The spatial–temporal C_p distributions of these four cases are shown in Figs. 31(c)–31(f). In the mixed-mode cases, the C_p fields reveal either underdeveloped DSV and TEV structures (as in $\overline{\alpha}15\Delta5k0.05$) or strong, competing contributions from both vortices (as in $\overline{\alpha}15\Delta5k0.16$ and $\overline{\alpha}15\Delta5k0.21$). In contrast, for $\overline{\alpha}15\Delta5k0.1$, the TEV remains underdeveloped while the DSV exhibits a well-defined suction region throughout its formation period, indicating dominance of the DSV dynamics. This case demonstrates that flow regime transitions are governed not solely by k, but by the combined effects of all three pitching parameters: mean angle of attack, amplitude, and reduced frequency.

In addition, it is also interesting to notice that at a very low reduced frequency of 0.05, both $\overline{\alpha}20\Delta15k0.05$ [Fig. 31(n)] and

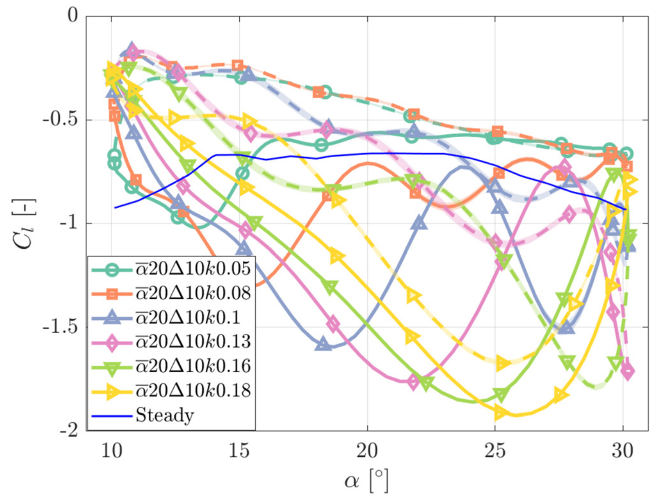

FIG. 23. C_l hystereses loops at different k values at $\overline{\alpha} = 20°$ and $\Delta\alpha = 10°$. The 95% confidence intervals are plotted together for each case as a shaded area. Due to very low uncertainty, these shaded areas are thin. The upstroke period is plotted in solid lines, and the downstroke period is plotted in dashed lines.

TABLE IV. Energy distribution of the most dominant mode(s) across conventional dynamic stall cases, grouped by $\overline{\alpha'}$.

Case	E_1 (%)	E_2 (%)
$\overline{\alpha'}5\Delta10k0.05$	96.7	2.8
$\overline{\alpha'}5\Delta10k0.1$	97.2	2.2
$\overline{\alpha'}5\Delta10k0.16$	97.4	2.1
$\overline{\alpha'}5\Delta15k0.05$	87.7	7.0
$\overline{\alpha'}5\Delta15k0.1$	90.3	4.0
$\overline{\alpha'}5\Delta15k0.16$	93.0	2.6
$\overline{\alpha'}10\Delta5k0.05$	96.7	2.1
$\overline{\alpha'}10\Delta5k0.1$	95.7	3.0
$\overline{\alpha'}10\Delta5k0.16$	95.1	3.7
$\overline{\alpha'}10\Delta5k0.21$	95.0	4.0
$\overline{\alpha'}10\Delta10k0.05$	89.8	6.3
$\overline{\alpha'}10\Delta10k0.1$	88.7	6.9
$\overline{\alpha'}10\Delta10k0.16$	89.2	6.0
$\overline{\alpha'}10\Delta15k0.05$	85.7	9.5
$\overline{\alpha'}10\Delta15k0.1$	85.4	9.4
$\overline{\alpha'}10\Delta15k0.16$	87.5	7.1
$\overline{\alpha'}15\Delta5k0.05$	88.9	6.1
$\overline{\alpha'}15\Delta5k0.1$	85.0	8.9
$\overline{\alpha'}15\Delta5k0.16$	83.8	9.8
$\overline{\alpha'}15\Delta5k0.21$	82.8	10.0
$\overline{\alpha'}15\Delta10k0.05$	78.7	14.4
$\overline{\alpha'}15\Delta10k0.1$	75.7	17.0
$\overline{\alpha'}15\Delta10k0.16$	79.1	13.5
$\overline{\alpha'}15\Delta14k0.05$	76.1	17.8
$\overline{\alpha'}15\Delta14k0.1$	76.5	16.5
$\overline{\alpha'}15\Delta14k0.16$	81.1	12.0

$\overline{\alpha}25\Delta15k0.05$ [Fig. 31(r)] exhibit a TEV-dominated flow. For these cases, due to larger pitching amplitudes, the trailing edge region experiences a longer suction period due to flow separation, even though the TEV is not present.

From this analysis, it can be concluded that the mean angle of attack is the main parameter that determines the dominant flow regime. In contrast, the effects of reduced frequency (k) and pitching amplitude ($\Delta\alpha$) are also important, but their influence is neither direct nor linear. Instead, the dominant flow regime emerges from the specific combination of pitching parameters, which governs the development patterns of the DSV and TEV on the airfoil surface. These patterns, such as underdeveloped vortices, multiple separation events, or strong competing DSV and TEV structures, directly define the prevailing flow regime.

D. Comparison with POD analysis from conventional dynamic stall

In order to further investigate the difference between conventional and reverse flow dynamic stall, the POD analysis was conducted on conventional dynamic stall cases tested in this campaign. Similar to the reverse flow case, the suction side C_p distribution was used in the analysis. Table IV shows the energy content of the first two dominant modes for all conventional dynamic stall cases. The result shows a universal trend across all tested conventional dynamic stall cases: the first mode has a dominant energy content of more than 75% of the total energy, while the second mode has much less energy, with a maximum of less than 20%. This means that for conventional dynamic stall cases, the pitching parameters of mean angle of attack, pitching amplitude, and pitching frequency do not alter the most energetic flow feature.

From the energy distribution, it is confirmed that the first mode is the dominant mode for conventional cases. The mode shape of the first mode for all conventional cases is shown in Fig. 24. Across all cases, the mode shapes of the first modes all present the same pattern, where the peak is shown at the leading edge with high concentration. In order to further confirm the relationship between the mathematical structures of the dominant POD mode (mode 1) and the physical dynamics in the flow field, the suction side C_p at case $\alpha'10\Delta\alpha10k0.16$ is reconstructed with the first mode. The result is shown in Fig. 25. The reconstructed C_p in the chordwise distribution [Fig. 25(a)] exhibits decreasing (or increasing) C_p from near the mid chord ($x_c/c = 0.6$) to the leading edge ($x_c/c = 0$), and the variation is the largest close to the leading edge. The spatial-temporal reconstructed field shows low C_p concentration stemming from the leading edge, appearing between $\alpha' = 11°$ during upstroke and $\alpha' = 16°$ during downstroke. This range also aligns with the extreme low-pressure region (LSB) shown at the leading edge in Fig. 11. Therefore, it is concluded that the dominant mode (mode 1) is related to the growth and decay of the leading edge negative pressure. Similar flow patterns can also be found in the conventional dynamic stall analysis from Li and Feng.[40]

Therefore, due to the presence of the LSBs, the dominant flow pattern exhibits uniform dominance dynamics near the leading edge for conventional dynamic stall cases. This result differs from the reverse flow dynamic stall cases, where the dominant energy can come from the dynamics of the DSV, TEV, or a mixture of both energies. This difference is fundamentally owing to the high suction from the LSB for conventional cases, and the gradual decrease in C_p at the initial stage of DSV formation for the reverse flow conditions.

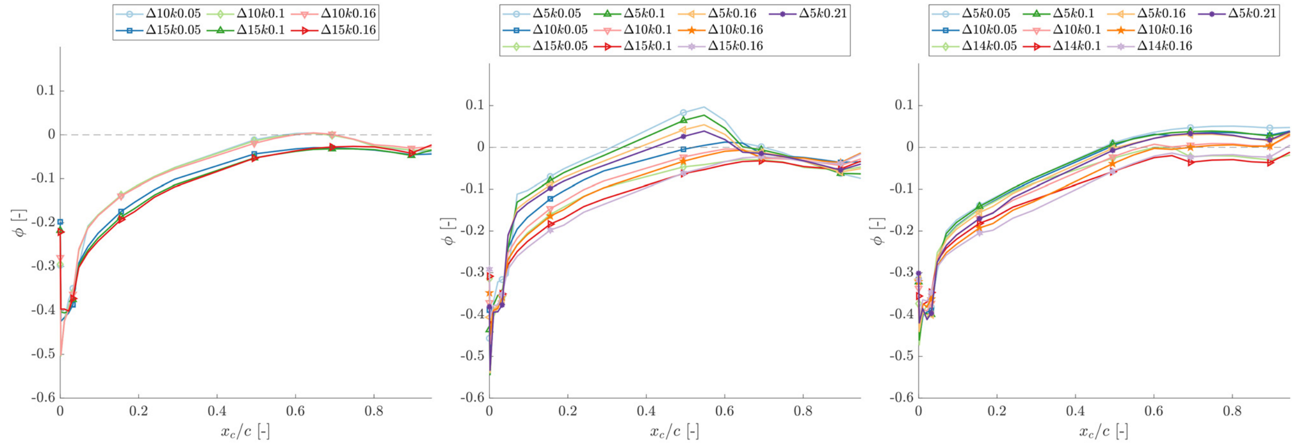

(a) $\overline{\alpha'} = 5°$ (b) $\overline{\alpha'} = 10°$ (c) $\overline{\alpha'} = 15°$

FIG. 24. POD mode shapes of the most dominant mode (mode 1) for conventional dynamic stall cases.

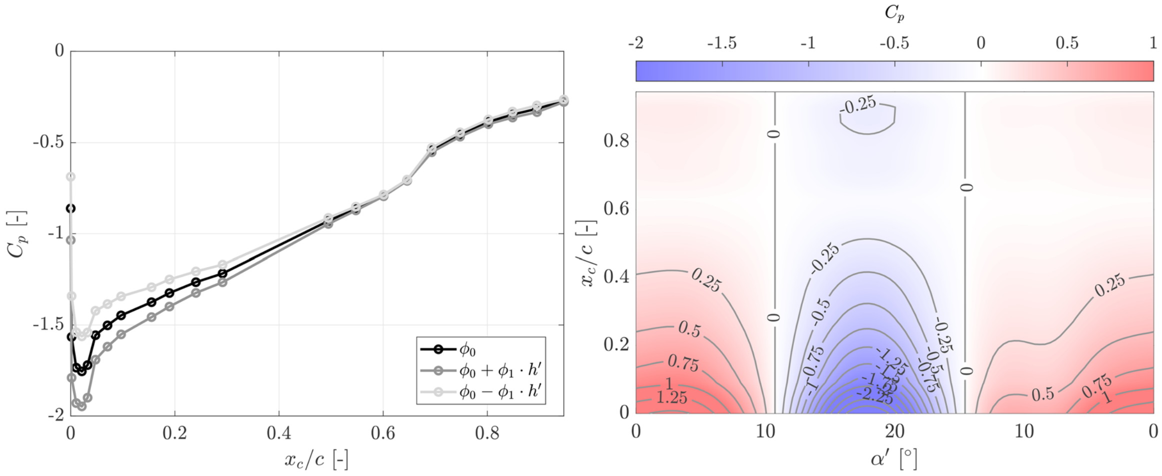

(a) (b)

FIG. 25. Reconstructed C_p chordwise distribution (left) and reconstructed C_p spatial–temporal field (right) from the first mode for case $\overline{\alpha}10\Delta10k0.16$.

IV. CONCLUSION

The dynamic stall of a pitching airfoil under reverse flow conditions is experimentally studied under different test parameters of mean angle of attack, reduced frequency, and pitching amplitude. Combining both surface pressure measurements and PIV flow field measurements, the analysis targets the relation between vortex evolution and aerodynamic force variation and the strong dominant flow features under different pitching cases.

Combined surface pressure and PIV flow fields provide detailed information on the vortex dynamics and their influence on the surface pressure. The multiple suction peaks on the airfoil suction side, instead of representing the number of DSVs generated during one pitching cycle, indicate that multiple DSV separations and shedding happen during a pitching cycle, which shows a universal trend among all the test cases. These separations are only partial: the outer part of the shear layer is shed downstream, while the inner part remains attached and feeds the circulation of the dynamic stall vortex. As a result, the force coefficient exhibits multiple peaks due to (1) DSV formation and partial separation and (2) the secondary growth of the attached DSV(s) and separation. Compared to conventional dynamic stall cases, the flow separation at the initial stage of DSV development causes a gradual decrease in the pressure coefficient. Instead, for conventional dynamic stall cases, the presence of the laminar separation bubbles leads to the suction peak near the leading edge region, before the DSV forms.[11,34,35]

In addition, POD analysis was conducted across all test cases to identify the dominant flow features. Over the tested parameter range ($k \in [0.05, 0.21]$, $\Delta\alpha \in [5°, 15°]$), the type of flow regime, and in

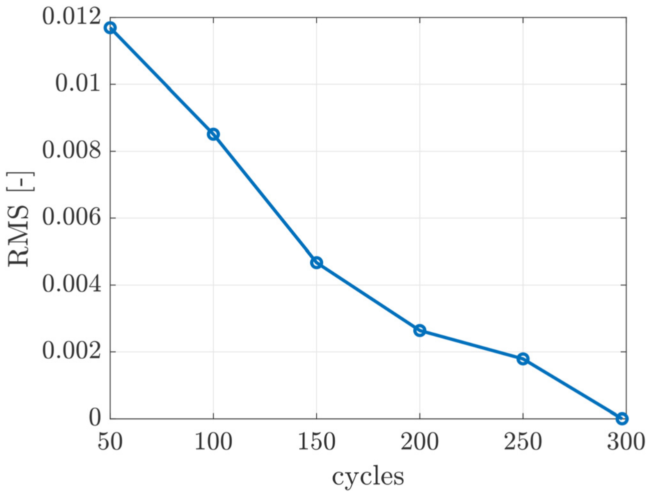

FIG. 26. Root mean square (RMS) of the trailing edge C_p compared to 298 cycles at $\overline{\alpha}' = 40^\circ$, $\Delta\alpha = 5^\circ$, $k = 0.11$.

particular, which vortex dominates the flow dynamics, depends mainly on the mean angle of attack $\overline{\alpha}$: (1) for low mean angle ($\overline{\alpha} = 5^\circ$ and 10°), the DSV development dominates the flow; for $\overline{\alpha} = 5^\circ$ cases, the TEV remains underdeveloped, with no discernible trailing-edge pressure peak. (2) For moderate mean angles ($\overline{\alpha} = 15^\circ$), the energy partitions comparably between DSV and TEV. (3) For high mean angle ($\overline{\alpha} = 20^\circ$ and 25°), multiple flow separations trigger robust TEV development, enabling more cases to have TEV dominance. Despite these $\overline{\alpha}$-dependent variations in modal dominance, all dominant POD modes share a consistent physical interpretation: they capture the growth or decay of DSV and TEV structures.

Finally, a POD analysis comparison was made between the conventional and reverse flow dynamic stall cases. It is shown that, similar to the literature,[40] for conventional dynamic stall cases, the most dominant energy (mode 1) represents the growth and decay of the leading edge negative pressure, which is highly related to the dynamics of the LSB(s). This most dominant energy shows the same pattern for all the conventional cases with different mean angles of attack, pitching amplitudes, and reduced frequencies. This result reveals the fundamental difference in the flow physics between conventional and reverse-flow dynamic stall. Such differences have important implications for real-world applications: for example, the strong partially attached DSVs or the TEV development under reverse flow can influence unsteady loading, vibration, and fatigue on parked wind turbine blades, propellers, and helicopter rotors, where reverse flow conditions are encountered.

ACKNOWLEDGMENTS

We would like to thank Stefan Bernardy for his technical support throughout the experimental campaign, Qingshen Meng for his help with the experiment matrix design, Pepijn Slooter and Abhratej Sahoo for their help during the wind tunnel campaign, and Mehdi Doosttalab for his help in the data post-processing.

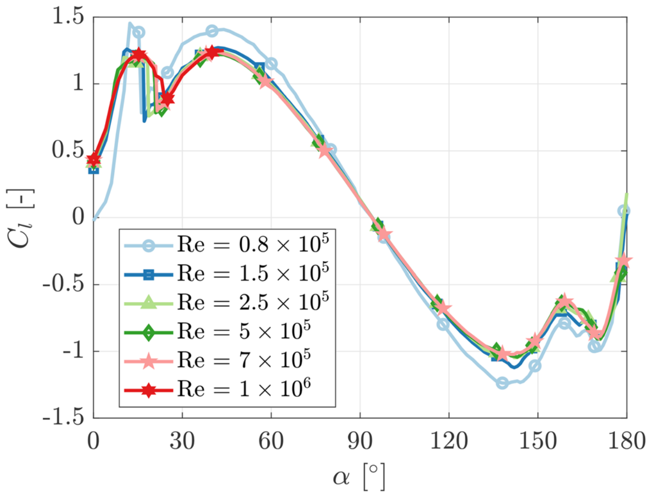

(a)

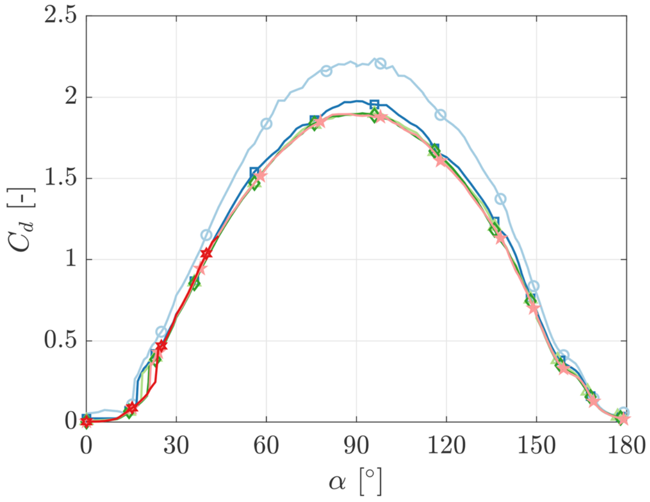

(b)

FIG. 27. Corrected C_l and C_d polars for all tested *Re*.

AUTHOR DECLARATIONS

Conflict of Interest

The authors have no conflicts to disclose.

Author Contributions

Guanqun Xu: Data curation (equal); Formal analysis (equal); Investigation (equal); Methodology (equal); Writing – original draft (equal). **Andrea Sciacchitano:** Conceptualization (equal); Formal analysis (equal); Methodology (equal); Supervision (equal); Writing – review & editing (equal). **Carlos Ferreira:** Conceptualization (equal); Formal analysis (equal); Methodology (equal); Supervision (equal); Writing – review & editing (equal). **Wei Yu:** Conceptualization (equal); Formal analysis (equal); Funding acquisition (equal); Methodology (equal); Supervision (equal); Writing – review & editing (equal).

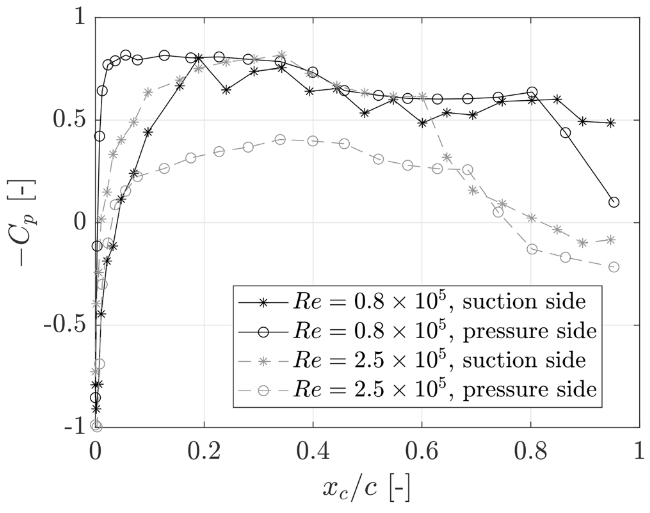

FIG. 28. C_p at $\alpha = 0°$ for $Re = 0.8 \times 10^5$ and 2.5×10^5.

DATA AVAILABILITY

The data that support the findings of this study are openly available in 4TU.ResearchData http://doi.org/10.4121/8cec2ee4-9dfa-47ba-a71d-69e73b625d38, Ref. 46.

APPENDIX A: EXPERIMENTAL DESIGN

1. Convergence analysis of pressure measurement

The NACA 643418 airfoil is selected for the pitching test. First, it is an asymmetric airfoil, which allows for a more representative simulation of wind turbine blade sections compared to symmetric sections. Second, this airfoil has been previously employed in wind energy with a few related studies,[41,42] providing a valuable benchmark and facilitating comparison of the present results with established research.

TABLE V. Aeroelastic simulation test cases.

Test case	$\overline{\alpha'}$ (°)	U_∞ (m/s)	St
1	35	24.1	0.16
2	90	42.0	0.16
3	135	15.9	0.16
4	160	14.4	0.16

TABLE VI. Blade tip pitch angle standard deviation δ and dominant frequency.

Test case	δ (°)	Peak frequency (Hz)	k
1	1.0	0.6,1.03	0.111,0.191
2	3.9	1.87	0.198
3	1.2	1.0	0.280
4	0.4	0.97	0.307

To determine the adequate cycle for data acquisition, a 299-cycle measurement was conducted for $\overline{\alpha'} = 40°$, $\Delta\alpha = 5°$, $k = 0.11$. Trailing edge data from cycles 50–298 were analyzed, excluding the first cycle to avoid transient effects. The root mean square error (RMS) compared to the 298-cycle case is shown in Fig. 26. Even for 50 cycles, RMS remains below 0.012, indicating good repeatability. To balance measurement efficiency and accuracy (RMS < 0.005), 150 cycles were used for pressure measurements and 50 cycles for PIV.

2. Selection of Reynolds number

To minimize Reynolds number effects on aerodynamic performance, static airfoil tests were conducted for Re ranging from 0.8×10^5 to 1×10^6. Pressure data were corrected for both dynamic response and wind tunnel wall effects (Sec. II C). Corrected C_l and C_d polars are shown in Fig. 27.

At the lowest $Re = 0.8 \times 10^5$, C_l at $\alpha = 0°$ is near zero, in contrast to approximately 0.4 for higher Re cases. The C_p distribution at $\alpha = 0°$ (Fig. 28) shows that the pressure difference between suction and pressure sides is negligible beyond $x/c = 0.2$ for $Re = 0.8 \times 10^5$, explaining the near-zero lift. At $Re = 1.5 \times 10^5$, deviations are observed in C_l (40°–60°, 120°–140°) and C_d (40°–150°). For $Re \geq 2.5 \times 10^5$, polars converge, stall regions smooth out, and Re effects are minimal. Therefore, $Re = 2.5 \times 10^5$ was selected for unsteady pressure measurements.

3. Pitching amplitude and frequency selection

Aeroelastic simulations of the NREL 5 MW wind turbine,[43] including a semi-empirical VIV model,[44,45] were used to determine suitable pitching amplitudes and frequencies for the experimental campaign. The model introduces an additional lift coefficient increment ΔC_l to account for VIV effects, defined as

$$\Delta C_l = \min\left(\max\left(3 - 2.4\frac{V_{crit,i}}{V_{m,Li}}\right), 1\right) C_{lat,0}, \tag{A1}$$

and the corresponding total lift on a blade section is

$$l(t) = \frac{1}{2}\rho U_\infty^2 D(\Delta C_l \cos(\Omega t) + C_l), \tag{A2}$$

TABLE VII. Relevant natural frequencies of the NREL 5-MW wind turbine.

Mode	Name	Frequency (Hz)
1	1st Drivetrain Torsion	0.6205
2	1st Blade Asymmetric Flapwise Yaw	0.6664
3	1st Blade Asymmetric Flapwise Pitch	0.6675
4	1st Blade Collective Flap	0.6993
5	1st Blade Asymmetric Edgewise Pitch	1.0793
6	1st Blade Asymmetric Edgewise Yaw	1.0898
7	2nd Blade Asymmetric Flapwise Yaw	1.9337
8	2nd Blade Asymmetric Flapwise Pitch	1.9223

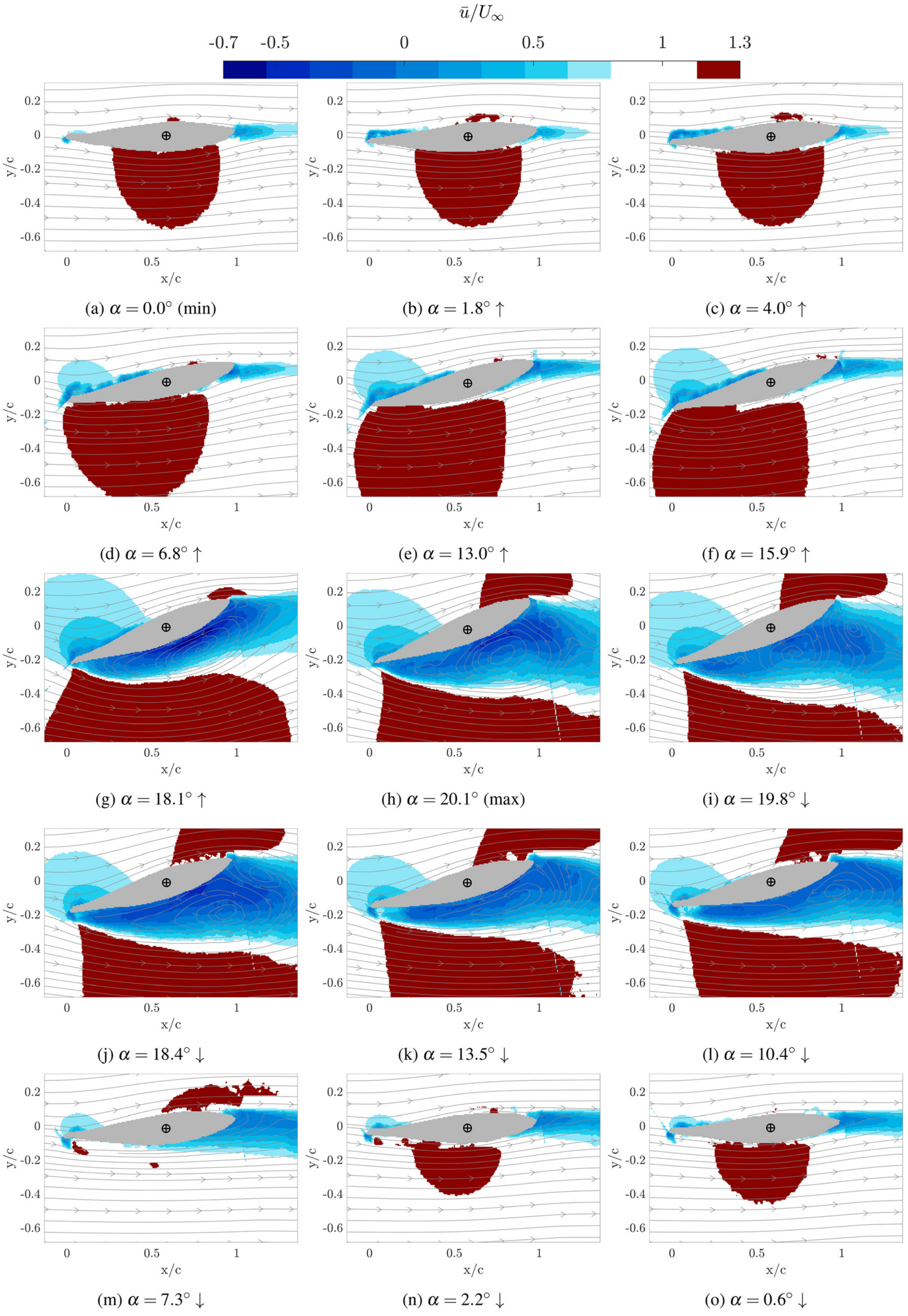

FIG. 29. Streamwise velocity field $\overline{U}/U_\infty$ for case $\overline{\alpha}10\Delta10k0.1$.

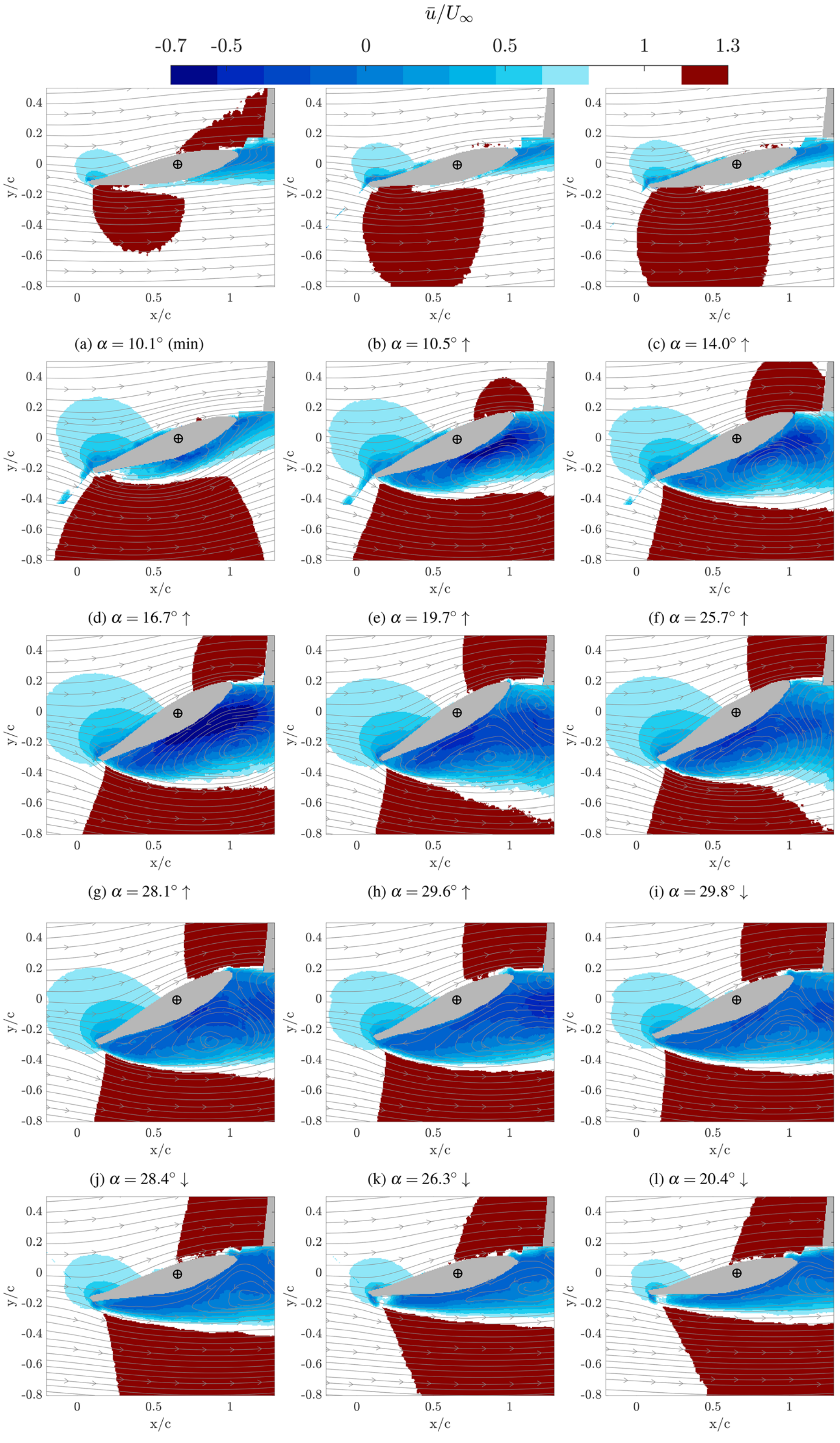

(a) $\alpha = 10.1°$ (min) (b) $\alpha = 10.5° \uparrow$ (c) $\alpha = 14.0° \uparrow$

(d) $\alpha = 16.7° \uparrow$ (e) $\alpha = 19.7° \uparrow$ (f) $\alpha = 25.7° \uparrow$

(g) $\alpha = 28.1° \uparrow$ (h) $\alpha = 29.6° \uparrow$ (i) $\alpha = 29.8° \downarrow$

(j) $\alpha = 28.4° \downarrow$ (k) $\alpha = 26.3° \downarrow$ (l) $\alpha = 20.4° \downarrow$

(m) $\alpha = 17.3° \downarrow$ (n) $\alpha = 14.5° \downarrow$ (o) $\alpha = 10.7° \downarrow$

FIG. 30. Streamwise velocity field $\overline{U}/U_\infty$ for case $\overline{\alpha}10\Delta10k0.1$.

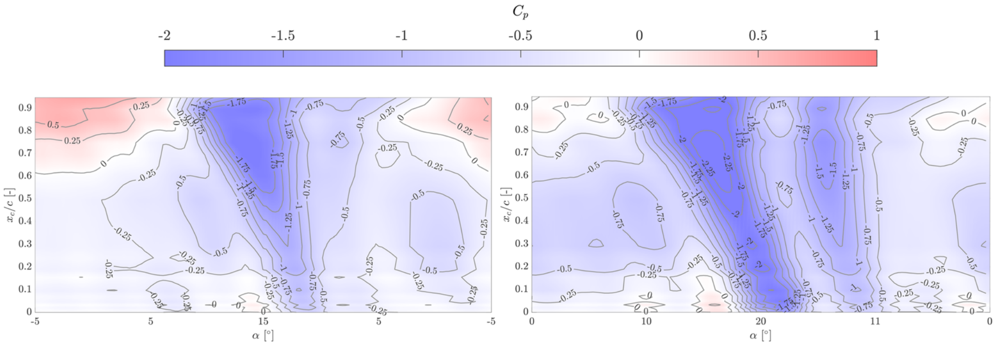

(a) $\overline{\alpha}5\Delta10k0.1$ (b) $\overline{\alpha}10\Delta10k0.13$

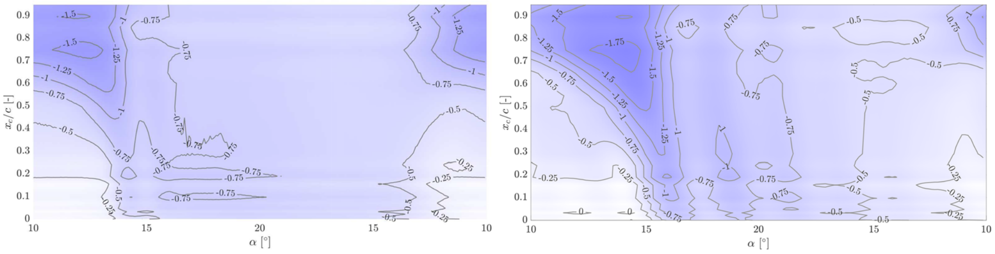

(c) $\overline{\alpha}15\Delta5k0.05$ (d) $\overline{\alpha}15\Delta5k0.1$

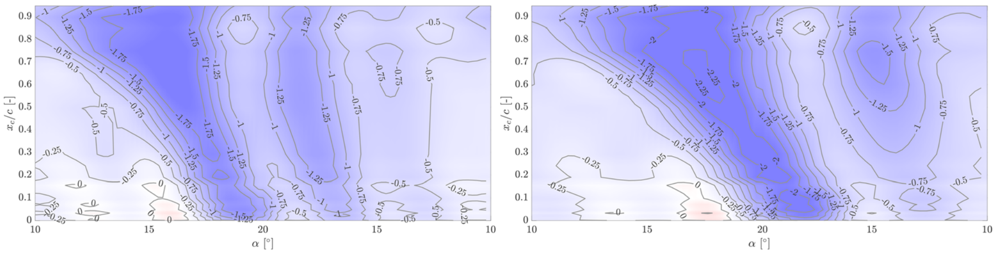

(e) $\overline{\alpha}15\Delta5k0.16$ (f) $\overline{\alpha}5\Delta5k0.21$

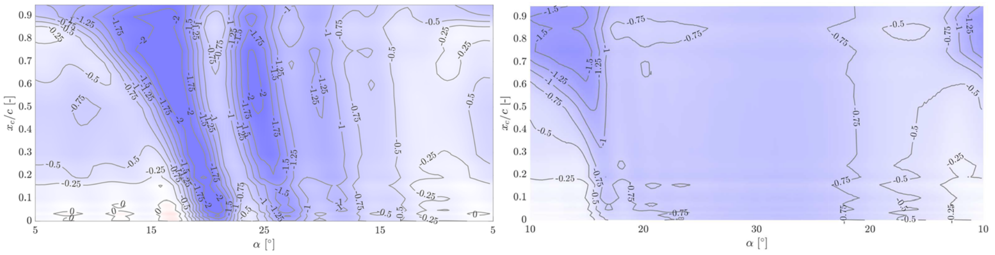

(g) $\overline{\alpha}15\Delta10k0.1$ (h) $\overline{\alpha}20\Delta10k0.05$

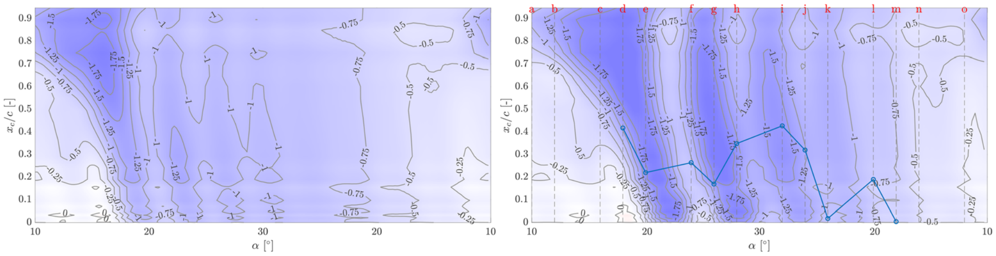

(i) $\overline{\alpha}20\Delta10k0.08$ (j) $\overline{\alpha}20\Delta10k0.1$

FIG. 31. Spatial–temporal field of suction side surface pressure coefficient C_p at representative cases.

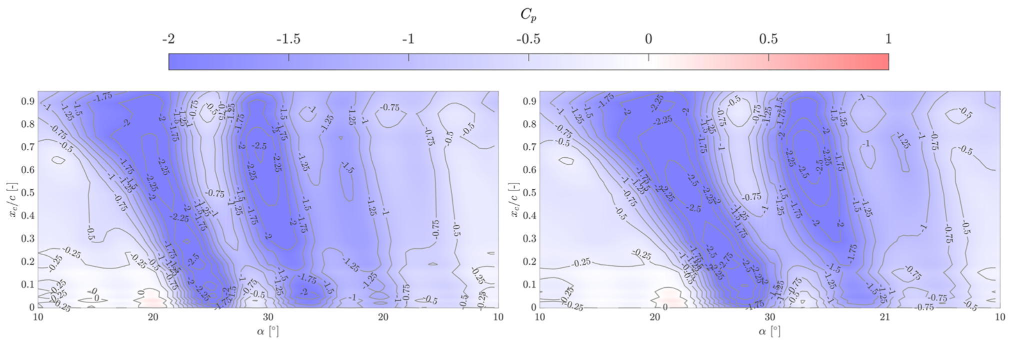

(k) $\overline{\alpha}20\Delta10k0.13$ (l) $\overline{\alpha}20\Delta10k0.16$

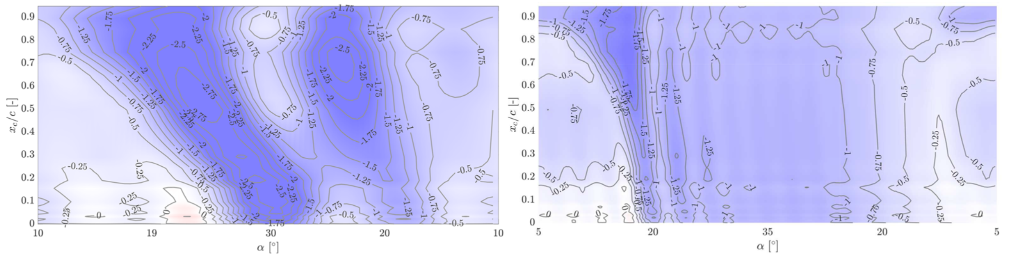

(m) $\overline{\alpha}20\Delta10k0.18$ (n) $\overline{\alpha}20\Delta15k0.05$

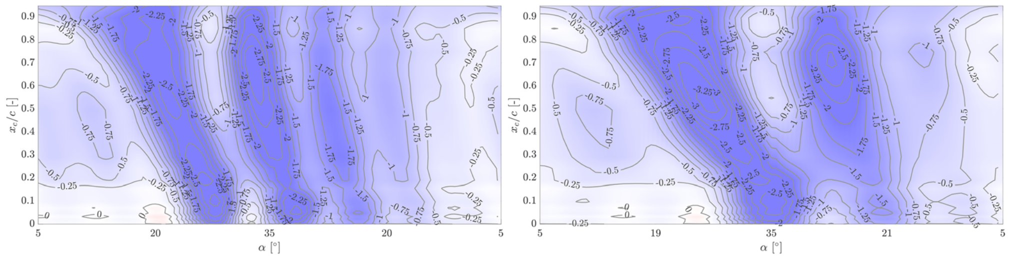

(o) $\overline{\alpha}20\Delta15k0.1$ (p) $\overline{\alpha}20\Delta15k0.16$

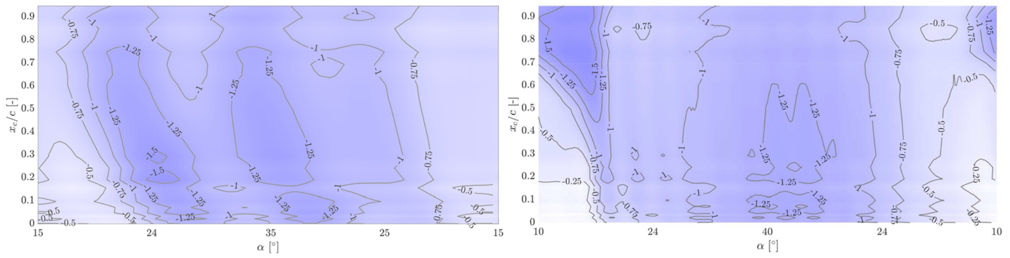

(q) $\overline{\alpha}25\Delta10k0.18$ (r) $\overline{\alpha}25\Delta15k0.05$

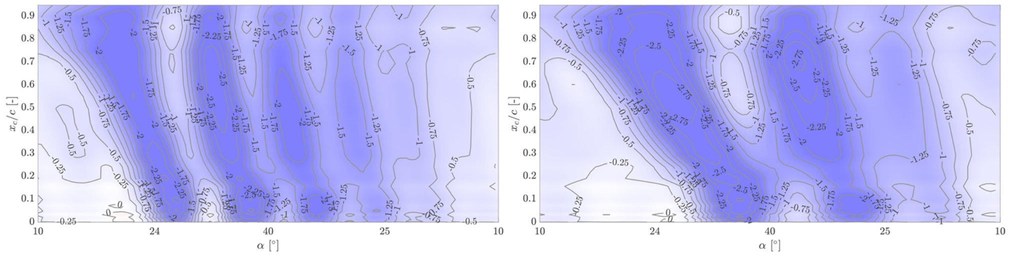

(s) $\overline{\alpha}25\Delta15k0.1$ (t) $\overline{\alpha}25\Delta15k0.16$

FIG. 31. (*Continued.*)

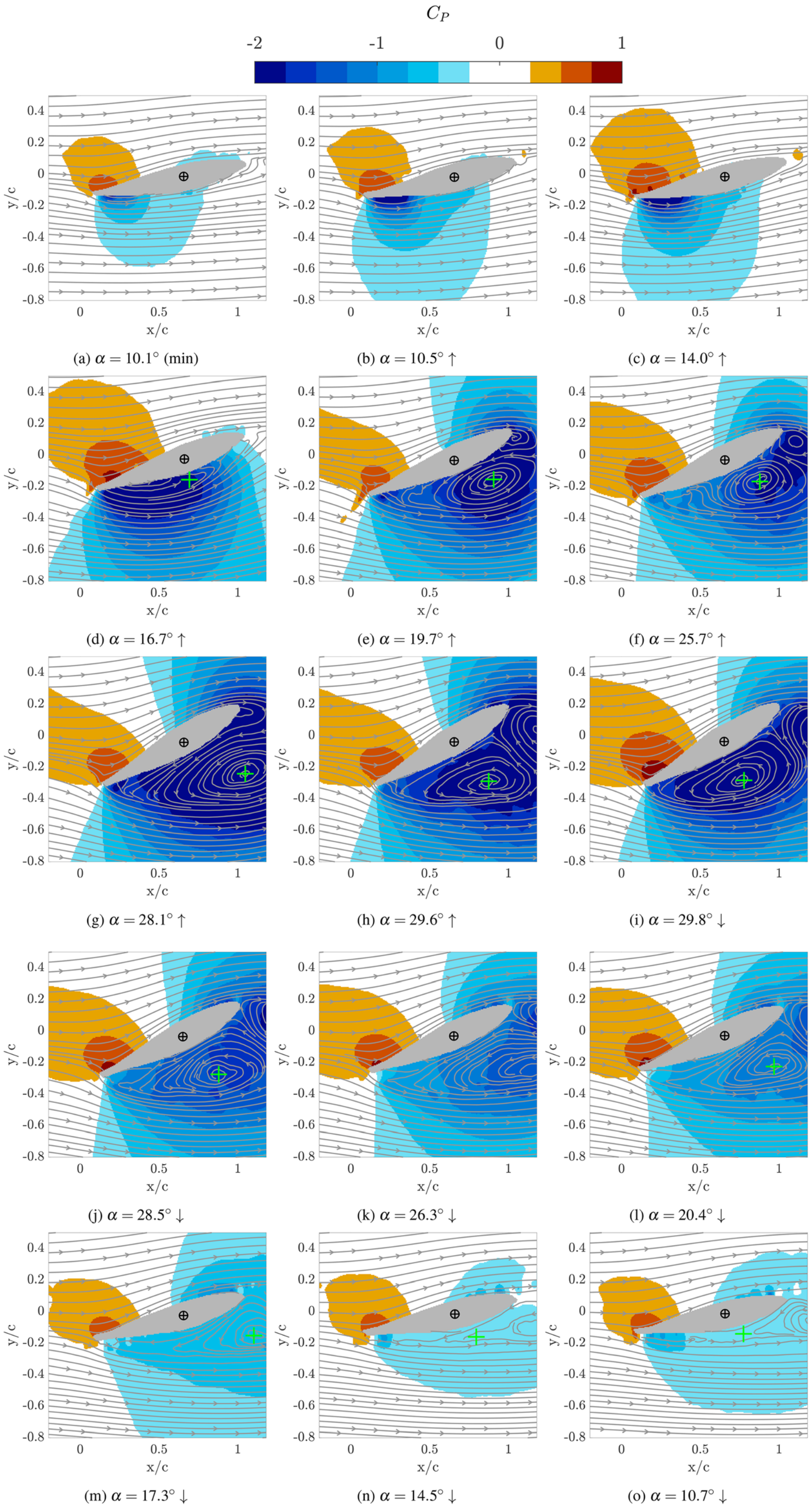

FIG. 32. Pressure coefficient field C_p for case $\overline{\alpha}20\Delta10k0.1$ obtained from PIV. Green cross represents the location of DSV core center, identified using Γ_1 method.[30,31]

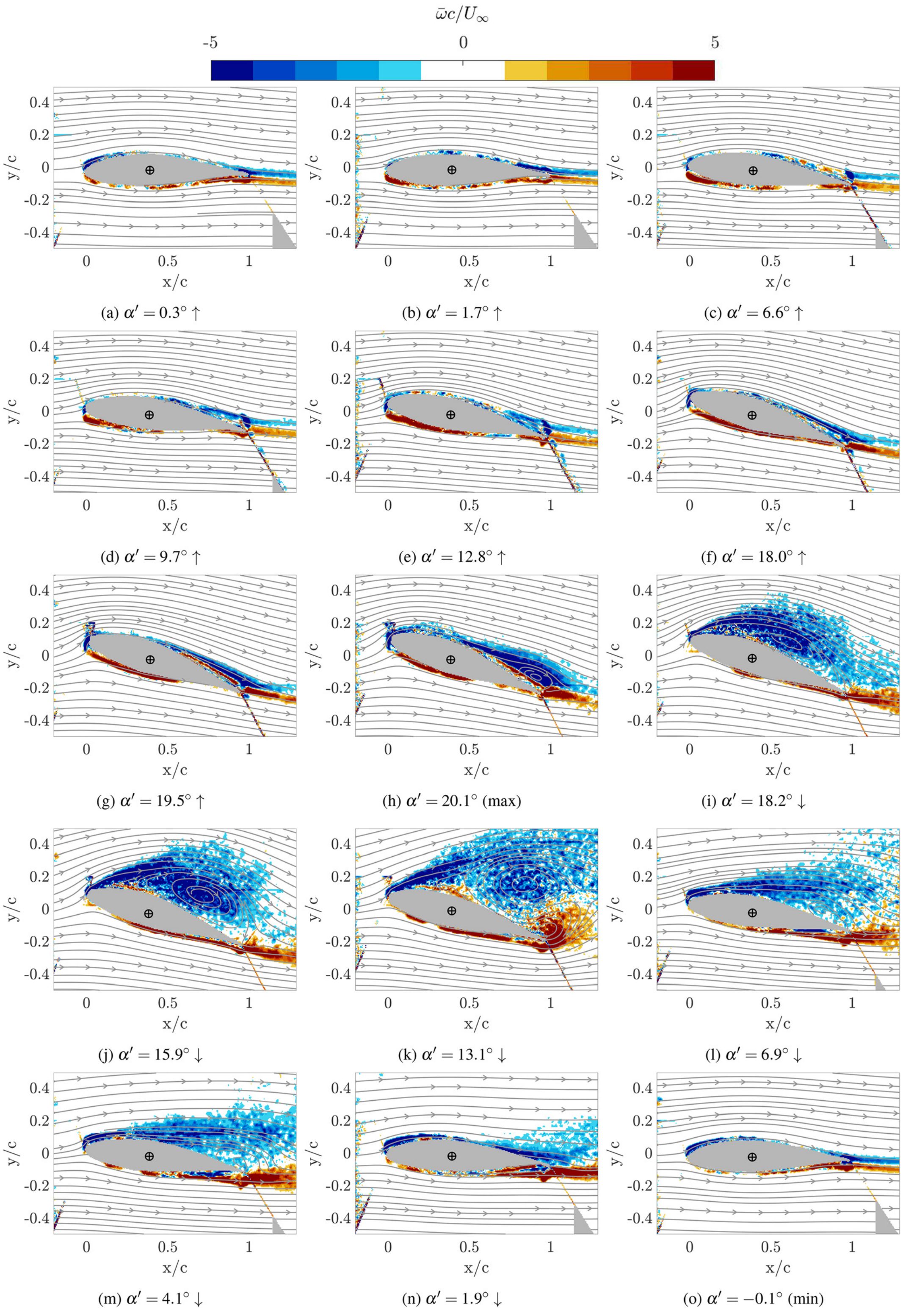

(a) $\alpha' = 0.3°$ ↑ (b) $\alpha' = 1.7°$ ↑ (c) $\alpha' = 6.6°$ ↑

(d) $\alpha' = 9.7°$ ↑ (e) $\alpha' = 12.8°$ ↑ (f) $\alpha' = 18.0°$ ↑

(g) $\alpha' = 19.5°$ ↑ (h) $\alpha' = 20.1°$ (max) (i) $\alpha' = 18.2°$ ↓

(j) $\alpha' = 15.9°$ ↓ (k) $\alpha' = 13.1°$ ↓ (l) $\alpha' = 6.9°$ ↓

(m) $\alpha' = 4.1°$ ↓ (n) $\alpha' = 1.9°$ ↓ (o) $\alpha' = -0.1°$ (min)

FIG. 33. Vorticity field $\overline{\omega}c/U_\infty$ for case $\overline{\alpha}' = 10°$, $\Delta\alpha = 10°$, $k = 0.16$.

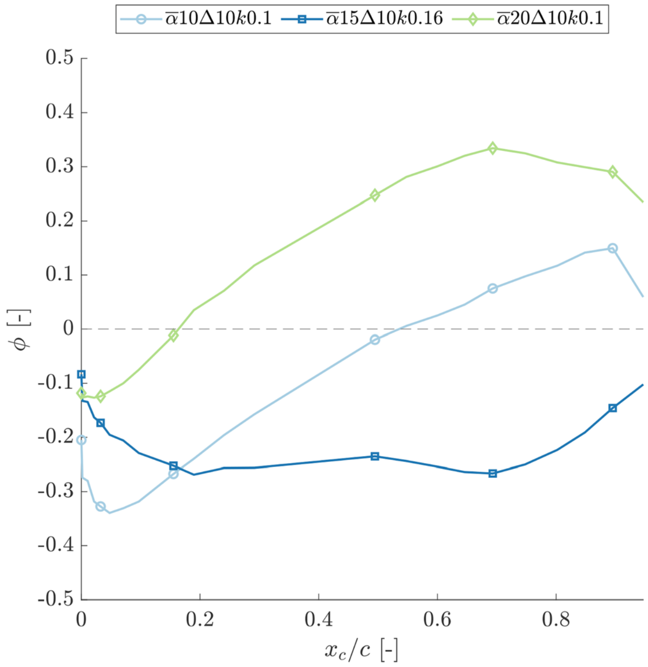

FIG. 34. POD mode shapes of the second dominant mode (mode 2) at three representative cases.

where ρ is air density, U_∞ is free stream wind speed, D is the projected chord, Ω corresponds to the Strouhal number, and C_l is the static lift coefficient at the instantaneous angle of attack.

Simulations were conducted for four mean pitch angles (35°, 90°, 135°, 160°) with wind speeds chosen to maintain $St \approx 0.16$ (Table V). Blade tip pitch angle time series were analyzed, showing standard deviations and dominant frequencies summarized in Table VI. The dominant frequencies overlap with natural modes of the turbine (Table VII), which clearly indicates the potential for VIV excitation.

Based on these results, experimental pitching amplitudes of 5°, 10°, and 15° were selected for each mean angle of attack, with testing frequencies between 1 and 4 Hz, corresponding to reduced frequencies $k = 0.05$–0.21. The upper frequency limit is determined by the wind tunnel pitching mechanism. This selection ensures that the experiments reproduce the angular variations and unsteady effects observed in the aeroelastic simulations while remaining within experimental constraints.

APPENDIX B: STREAMWISE VELOCITY FIELD AT TWO REPRESENTATIVE CASES

Figures 29 and 30 present the streamwise velocity field $\overline{U}/U_\infty$ at case $\overline{\alpha}10\Delta10k0.1$ and $\overline{\alpha}20\Delta10k0.1$, respectively, in order to provide more information apart from the vorticity field shown in Figs. 7 and 14. For both cases, the results show that as the airfoil pitches up, the wake becomes wider: at case $\overline{\alpha}10\Delta10k0.1$, a thin layer of reverse flow region (deep blue color) occurs on the suction side (see phases j and h), while for the high mean angle case of $\overline{\alpha}20\Delta10k0.1$, the suction region occurs earlier from phase d and the wake is also wider. During the downstroke period, the wake in case $\overline{\alpha}10\Delta10k0.1$ recovers quickly, while for case $\overline{\alpha}20\Delta10k0.1$, the wake remains wide until the end of the downstroke cycle due to a high angle of attack. This PIV result also matches the pressure measurement in that, due to a high mean angle, the suction pressure is higher for $\overline{\alpha}20\Delta10k0.1$ [Fig. 13(a)], which also leads to a higher aerodynamic force (Fig. 15). Noticeably, the reverse flow region is concentrated near the trailing edge for case $\overline{\alpha}20\Delta10k0.1$ at phases f, g, and k, for example, while no strong reverse flow can be found near the trailing edge at case $\overline{\alpha}10\Delta10k0.1$. This result further indicates that in case $\overline{\alpha}20\Delta10k0.1$, the TEV has a stronger strength, which leads to the TEV domination as discussed in Sec. III B.

APPENDIX C: SPATIAL-TEMPORAL FIELD OF SUCTION SIDE C_p FOR A FEW REPRESENTATIVE CASES

In this section, the cycle-averaged suction side C_p for a few representative is presented in Fig. 31. The maps are plotted with a universal C_p range from -2 to 1. The gray contour lines indicate the C_p magnitude with an increment of 0.25.

APPENDIX D: C_p FIELD OBTAINED FROM PIV MEASUREMENT FOR CASE $\overline{\alpha}20\Delta10k0.1$

Figure 32 presents the C_p field at case $\overline{\alpha}20\Delta10k0.1$ extracted from the PIV measurement.

APPENDIX E: VORTICITY FIELD $\overline{\omega}c/U_\infty$ AT A CONVENTIONAL DYNAMIC STALL CASE $\overline{\alpha}'10\Delta10k0.16$: $\overline{\alpha}'=10°$, $\Delta\alpha=10°$, $k=0.16$

The vorticity field of the conventional dynamic stall case $\overline{\alpha}'10\Delta10k0.16$ is presented in Fig. 33.

APPENDIX F: THE SECOND POD MODE SHAPES FOR REPRESENTATIVE REVERSE FLOW TEST CASES

Figure 34 shows the mode shape from the second mode for three cases that represent the three different flow regimes from POD analysis separately. Specifically, $\overline{\alpha}10\Delta10k0.1$ is the representative case for the DSV-dominated flow, $\overline{\alpha}15\Delta10k0.16$ is the representative case for the mixed energy flow, and $\overline{\alpha}20\Delta10k0.1$ is the representative case for the TEV-dominated flow.

REFERENCES

[1] L. W. Carr, "Progress in analysis and prediction of dynamic stall," J. Aircraft **25**, 6–17 (1988).
[2] W. J. McCroskey and R. K. Fisher, "Detailed aerodynamic measurements on a model rotor in the blade stall regime," Report No. AHS PREPRINT 521 (1972).
[3] W. J. McCroskey, "The phenomenon of dynamic stall," Technical Report NASA TM-81264 (1981).
[4] K. W. McAlister, L. W. Carr, and W. J. Mccroskey, "Dynamic stall experiments on the NACA 0012 airfoil," Technical Report NASA-TP-1100 (1978).
[5] J. G. Leishman and T. S. Beddoes, "A semi-empirical model for dynamic stall," J. Am. Helicopter Soc. **34**, 3–17 (1989).

[6] V. K. Truong, "A 2-D dynamic stall model based on a Hopf bifurcation," Technical Report C23 (1993).
[7] C. T. Tran and D. Petot, "Semi-empirical model for the dynamic stall of airfoils in view to the application to the calculation of responses of a helicopter blade in forward flight," Vertica **5**(1), 35–53 (1980).
[8] M. H. Akbari and S. J. Price, "Simulation of dynamic stall for a NACA 0012 airfoil using a vortex method," J. Fluids Struct. **17**, 855–874 (2003).
[9] K. Mulleners and M. Raffel, "The onset of dynamic stall revisited," Exp. Fluids **52**, 779–793 (2012).
[10] K. Mulleners and M. Raffel, "Dynamic stall development," Exp. Fluids **54**(2), 1–9 (2013).
[11] R. Gupta and P. J. Ansell, "Unsteady flow physics of airfoil dynamic stall," AIAA J. **57**, 165–175 (2019).
[12] J. Kiefer, C. E. Brunner, M. O. Hansen, and M. Hultmark, "Dynamic stall at high Reynolds numbers induced by ramp-type pitching motions," J. Fluid Mech. **938**, A10 (2022).
[13] A. Datta, H. Yeo, and T. R. Norman, "Experimental investigation and fundamental understanding of a full-scale slowed rotor at high advance ratios," J. Am. Helicopter Soc. **58**, 1–17 (2013).
[14] M. Potsdam, A. Datta, and B. Jayaraman, "Computational investigation and fundamental understanding of a slowed UH-60A rotor at high advance ratios," J. Am. Helicopter Soc. **61**, 1 (2016).
[15] N. Guillaud, G. Balarac, and E. Goncalvès, "Large eddy simulations on a pitching airfoil: Analysis of the reduced frequency influence," Computers Fluids **161**, 1–13 (2018).
[16] G. J. Leishman, *Principles of Helicopter Aerodynamics* (Cambridge University Press, 2006).
[17] B. Wei, Y. Gao, and D. Li, "Physics of dynamic stall vortex during pitching oscillation of dynamic airfoil," Int. J. Aeronaut. Space Sci. **22**, 1263–1277 (2021).
[18] N. M. Khalifa, A. Rezaei, and H. E. Taha, "On computational simulations of dynamic stall and its three-dimensional nature," Phys. Fluids **35**, 105143 (2023).
[19] A. H. Lind and A. R. Jones, "Unsteady aerodynamics of reverse flow dynamic stall on an oscillating blade section," Phys. Fluids **28**, 077102 (2016).
[20] J. D. Anderson, *Fundamentals of Aerodynamics* (McGraw Hill, 2011).
[21] Student, "The probable error of a mean," Biometrika **6**, 1 (1908).
[22] A. Sciacchitano and F. Scarano, "Elimination of PIV light reflections via a temporal high pass filter," Meas. Sci. Technol. **25**, 084009 (2014).
[23] Q. Ye, F. F. Schrijer, and F. Scarano, "Boundary layer transition mechanisms behind a micro-ramp," J. Fluid Mech. **793**, 132–161 (2016).
[24] A. Sciacchitano and B. Wieneke, "PIV uncertainty propagation," Meas. Sci. Technol. **27**, 084006 (2016).
[25] H. Bergh and H. Tijdeman, "Theoretical and experimental results for the dynamic response of pressure measuring systems," Technical Report NLR-TR F.238 (1965).
[26] G. Xu, W. Yu, C. Ferreira, A. Sciacchitano, and S. Iyer, "Experimental comparison of a NACA0021 airfoil in large plunging and surging motions at 90° angle of attack," J. Phys. Conf. Ser. **2767**, 022047 (2024).
[27] W. A. Timmer, "Wind tunnel wall corrections for two-dimensional testing up to large angles of attack," in Handbook of Wind Energy Aerodynamics (Springer International Publishing, 2022) pp. 601–629.
[28] E. C. Maskell, "A theory of the blockage effects on bluff bodies and stalled wings in a closed wind tunnel," Technical Report AD-A955 243 (1963).
[29] A. Chatterjee, "An introduction to the proper orthogonal decomposition," Technical Report 7 (2000).
[30] L. Graftieaux, M. Michard, and N. Grosjean, "Combining PIV, POD and vortex identification algorithms for the study of unsteady turbulent swirling flows," Meas. Sci. Technol. **12**, 1422 (2001).
[31] C. E. Morgan, H. Babinsky, and J. K. Harvey, "Vortex detection methods for use with PIV and CFD data," in *47th AIAA Aerospace Science Meeting Including New Horizons Forum Aerospace Exposition* (AIAA, 2009).
[32] B. W. Van Oudheusden, "PIV-based pressure measurement," Meas. Sci. Technol. **24**, 032001 (2013).
[33] G. Xu, A. Sciacchitano, C. Ferreira, and W. Yu, "On the unsteady aerodynamics of a surging airfoil at 90° incidence," Exp. Fluids **66**, 85 (2025).
[34] M. R. Visbal and S. I. Benton, "Exploration of high-frequency control of dynamic stall using large-eddy simulations," AIAA J. **56**, 2974–2991 (2018).
[35] S. Sudharsan, S. Narsipur, and A. Sharma, "Evaluating dynamic stall-onset criteria for mixed and trailing-edge stall," AIAA J. **61**, 1181–1196 (2023).
[36] M. R. Visbal, "Numerical exploration of flow control for delay of dynamic stall on a pitching airfoil," in *32nd AIAA Applied Aerodynamics Conference* (American Institute of Aeronautics and Astronautics Inc., 2014).
[37] J. Hodara, A. H. Lind, A. R. Jones, and M. J. Smith, "Collaborative investigation of the aerodynamic behavior of airfoils in reverse flow," J. Am. Helicopter Soc. **61**, 1 (2016).
[38] S. W. Kim, A. K. B. M. Q. Zaman, and J. Panda, "Numerical investigation of unsteady transitional flow over oscillating airfoil," J. Fluids Eng. **117**, 10 (1995).
[39] P. R. Hammer, D. J. Garmann, and M. R. Visbal, "Effect of aspect ratio on finite-wing dynamic stall," AIAA J. **60**, 6581–6593 (2022).
[40] X. Li and L. H. Feng, "Critical indicators of dynamic stall vortex," J. Fluid Mech. **937**, A16 (2022).
[41] D. Ragni and C. Ferreira, "Effect of 3D stall-cells on the pressure distribution of a laminar NACA64-418 wing," Exp. Fluids **57**, 127 (2016).
[42] E. Llorente and D. Ragni, "Trailing edge serrations effects on the aerodynamic performance of a NACA 643418," Wind Energy **22**, 392–406 (2019).
[43] J. Jonkman, S. Butterfield, W. Musial, and G. Scott, "Definition of a 5-MW reference wind turbine for offshore system development," Technical Report NREL/TP-500-38060 (2009).
[44] "EN 1991-1-4: Eurocode 1: Actions on structures—Part 1–4: General actions—Wind actions" (2005).
[45] D. I. Manolas, P. K. Chaviaropoulos, and V. A. Riziotis, "Assessment of vortex induced vibrations on wind turbines," J. Phys. Conf. Ser. **2257**, 012011 (2022).
[46] G. Xu, W. Yu, A. Sciacchitano, C. Ferreira, and P. Slooter (2024). "Data from the experimental measurement of a pitching airfoil NACA643418," 4TU.ResearchData, V. 2, Dataset. https://data.4tu.nl/datasets/8cec2ee4-9dfa-47ba-a71d-69e73b625d38/2